



# The ALMA Discovery of the Rotating Disk and Fast Outflow of Cold Molecular Gas in NGC 1275

H. Nagai<sup>1,2</sup>, K. Onishi<sup>3,4</sup>, N. Kawakatu<sup>5</sup>, Y. Fujita<sup>6</sup>, M. Kino<sup>1,7</sup>, Y. Fukazawa<sup>8</sup>, J. Lim<sup>9</sup>, W. Forman<sup>10</sup>, J. Vrtilik<sup>10</sup>, K. Nakanishi<sup>1,2</sup>, H. Noda<sup>6,14</sup>, K. Asada<sup>11</sup>, K. Wajima<sup>12</sup>, Y. Ohyama<sup>11</sup>, L. David<sup>10</sup>, and K. Daikuhara<sup>13</sup>

<sup>1</sup>National Astronomical Observatory of Japan, Osawa 2-21-1, Mitaka, Tokyo 181-8588, Japan; [hiroshi.nagai@nao.ac.jp](mailto:hiroshi.nagai@nao.ac.jp)

<sup>2</sup>The Graduate University for Advanced Studies (SOKENDAI), Osawa 2-21-1, Mitaka, Tokyo 181-8588, Japan

<sup>3</sup>Research Center for Space and Cosmic Evolution, Ehime University, 2-5 Bunkyo-cho, Matsuyama, Ehime 790-8577, Japan

<sup>4</sup>Department of Space, Earth and Environment, Chalmers University of Technology, Onsala Observatory, SE-439 92 Onsala, Sweden

<sup>5</sup>National Institute of Technology, Kure College, 2-2-11, Agaminami, Kure, Hiroshima, 737-8506, Japan

<sup>6</sup>Department of Earth and Space Science, Graduate School of Science, Osaka University, 1-1 Machikaneyama-cho, Toyonaka-shi, Osaka 560-0043, Japan

<sup>7</sup>Kogakuin University of Technology & Engineering, Academic Support Center, 2665-1 Nakano, Hachioji, Tokyo 192-0015, Japan

<sup>8</sup>Hiroshima University, 1-3-1 Kagamiyama, Higashi-Hiroshima 739-8526, Japan

<sup>9</sup>Department of Physics, The University of Hong Kong, Pokfulam Road, Hong Kong, People's Republic of China

<sup>10</sup>Harvard-Smithsonian Center for Astrophysics, 60 Garden Street, Cambridge, MA 02138, USA

<sup>11</sup>Institute of Astronomy and Astrophysics, Academia Sinica, 11F of Astronomy-Mathematics Building, AS/NTU, No.1, Sec. 4, Roosevelt Rd, Taipei 10617, Taiwan, People's Republic of China

<sup>12</sup>Korea Astronomy and Space Science Institute, 776 Daedeok-daero, Yuseong-gu, Daejeon 34055, Republic of Korea

<sup>13</sup>Department of Physics, Toho University, 2-2-1 Miyama, Funabashi, Chiba 274-8510, Japan

<sup>14</sup>Project Research Center for Fundamental Sciences, Graduate School of Science, Osaka University, 1-1 Machikaneyama-cho, Toyonaka, Osaka 560-0043, Japan

Received 2019 March 4; revised 2019 August 1; accepted 2019 August 25; published 2019 October 4

## Abstract

We present observations using the Atacama Large Millimeter/submillimeter Array of the CO(2–1), HCN(3–2), and HCO<sup>+</sup>(3–2) lines in the nearby radio galaxy/brightest cluster galaxy (BCG) NGC 1275 with a spatial resolution of  $\sim 20$  pc. In previous observations, the CO(2–1) emission was detected as radial filaments lying in the east–west direction on a kiloparsec scale. We resolved the inner filament and found that it cannot be represented by a simple infalling stream on a sub-kiloparsec scale. The observed complex nature of the filament resembles the cold gas structure predicted by numerical simulations of cold chaotic accretion. Within the central 100 pc, we detected a rotational disk of molecular gas whose mass is  $\sim 10^8 M_{\odot}$ . This is the first evidence of the presence of a massive cold gas disk on this spatial scale for BCGs. A crude estimate suggests that the accretion rate of the cold gas can be higher than that of hot gas. The disk rotation axis is approximately consistent with the radio-jet axis. This probably suggests that the cold gas disk is physically connected to the innermost accretion disk, which is responsible for jet launching. We also detected absorption features in the HCN(3–2) and HCO<sup>+</sup>(3–2) spectra against the radio continuum emission mostly radiated by a jet of size  $\sim 1.2$  pc. The absorption features are blueshifted from the systemic velocity by  $\sim 300$ – $600$  km s<sup>–1</sup>, suggesting the presence of outflowing gas from the active galactic nucleus (AGN). We discuss the relation of the AGN feeding with cold accretion, the origin of blueshifted absorption, and an estimate of the black hole mass using molecular gas dynamics.

**Key words:** galaxies: active – galaxies: elliptical and lenticular, cD – galaxies: individual (3C 84, NGC 1275, Perseus A) – galaxies: nuclei

## 1. Introduction

The Perseus cluster is a nearby ( $z = 0.017$ ) cluster of galaxies and has been the subject of extensive research over many years at all wavelengths. The cluster harbors the radio galaxy/brightest cluster galaxy (BCG) NGC 1275 at its center. Owing to its nuclear emission NGC 1275 was originally classified as a Seyfert 2 (Seyfert 1943) but it has since also been classified as a Seyfert 1.5/LINER (Sosa-Brito et al. 2001; Véron-Cetty & Véron 2006) because of the presence of a broad H $\alpha$  wing. The total luminosity in the 1990s was  $4 \times 10^{44}$  erg s<sup>–1</sup> (Levinson et al. 1995). This luminosity is about 0.4% of the Eddington luminosity for a black hole mass of  $8 \times 10^8 M_{\odot}$  (Scharwächter et al. 2013). The radio luminosity of this source is  $3 \times 10^{24}$  W Hz<sup>–1</sup> sr<sup>–1</sup> at 178 MHz, which classifies it as a Fanaroff–Riley I radio source (Fanaroff & Riley 1974).

This galaxy shows intermittent jet activity in which the most recent activity started in  $\sim 2005$  (Abdo et al. 2009; Nagai et al. 2010; Suzuki et al. 2012). This system is the brightest X-ray cluster of galaxies and one of the best examples of a prototypical

“cool core” cluster with a signature of the interaction between the jet and the intracluster medium (ICM) (e.g., Fabian et al. 2003). In contrast to other nearby BCGs such as M87 (Perlman et al. 2007; Tan et al. 2008), NGC 1275 is the reservoir of a large amount of cold gas ( $M_{\text{gas}} \simeq 10^{10} M_{\odot}$ ) with filamentary structures on kiloparsec scales (Salomé et al. 2006, 2008; Lim et al. 2008), which is reminiscent of a cooling flow. These properties make NGC 1275 the ideal target in which to study the feeding and feedback between the central supermassive black hole (SMBH) and the surrounding environment.

Despite extensive efforts, the gas fueling mechanism from the ICM to the SMBH is not yet clear. On kiloparsec scales, molecular gas filaments are aligned in the east–west direction (Lim et al. 2008) and those filaments seem to coincide with the H $\alpha$  nebulae (Fabian et al. 2008). While the gas kinematics in the outer filaments is consistent with the infalling motion, the inner filament of the molecular gas ( $M_{\text{gas}} \simeq 10^9 M_{\odot}$ ; Lim et al. 2008) cannot be explained by either a simple inflow or outflow, and thus it is not clear whether such a large amount of molecular gas is accreting to the center. On the other hand, the

circumnuclear disk (CND) is clearly resolved by the warm H<sub>2</sub> and ionized [Fe II] lines in the inner 50 pc, in both morphology and kinematics, with the Gemini Telescope (Scharwächter et al. 2013). It was suggested from the observed velocity dispersion that the H<sub>2</sub> emission traces the outer region of the disk, which is likely to form a toroid, while the [Fe II] line traces the inner region of the disk, which is illuminated by the ionizing photons from the active galactic nucleus (AGN). The inner ionized part is possibly associated with the “silhouette” disk, which is identified by the free–free absorption (FFA) of background synchrotron emission from the counter-jet by observations using very long baseline interferometry (VLBI) (e.g., Walker et al. 2000; Fujita & Nagai 2017). Fujita & Nagai (2017) measured the opacity of FFA ( $\tau_{\text{ff}}$ ) toward the counter-jet component in the central  $\sim 1$  pc region and found  $\tau_{\text{ff}} \propto \nu^{-0.6}$ , which is different from that for a uniform density,  $\tau_{\text{ff}} \propto \nu^{-2}$ . They argued that the absorbing medium is highly inhomogeneous and that it consists of regions with  $\tau_{\text{ff}} \ll 1$  and regions with  $\tau_{\text{ff}} \gg 1$ .

Numerical simulations of giant elliptical galaxies suggest that the mass accretion is dominated by chaotic cold accretion (CCA) within the inner kiloparsec (Barai et al. 2012; Gaspari et al. 2013). These simulations also predict that the CCA leads to a deflection of jets and strong variation in the AGN luminosity. Such a jet deflection and change in luminosity are indeed observed in NGC 1275/3C 84 in radio, X-ray, and  $\gamma$ -ray bands (Nagai et al. 2010; Dutson et al. 2014; Fabian et al. 2015), though the connection between different frequency bands is not well understood (Nagai et al. 2012, 2016; Hodgson et al. 2018). Thus, Gaspari’s simulation seems to represent the observed AGN properties of NGC 1275. Contrary to other elliptical galaxies in a cool-core cluster system, such as M87 (Forman et al. 2007), NGC 1275 indeed possesses a large amount of cold gas in the center ( $M_{\text{gas}} \sim 10^9 M_{\odot}$ ; Lazareff et al. 1989; Mirabel et al. 1989; Lim et al. 2008; Salomé et al. 2008). Salomé et al. (2011) discussed the possible presence of a CO molecular disk within 2 kpc. However, resolving the inner ( $< 1$  kpc) region has so far been difficult because of the lack of resolution at millimeter wavelengths. High-resolution observations of the cold molecular gas with the Atacama Large Millimeter/submillimeter Array (ALMA) are key to uncovering the missing link between the outer kiloparsec and the inner  $\lesssim 50$  pc, which is crucial to understanding of the mass accretion from the ICM to the SMBH.

In broader perspectives, it is also intriguing to study the relation of the observed CND with the AGN torus in terms of the unified scheme (Antonucci 1993). Although many studies have been done for prototypical Seyfert galaxies with ALMA in this regard (e.g., Imanishi et al. 2018), the properties of the CND and its relation to the AGN torus in BCG/radio galaxies are less clear. From theoretical studies, it is predicted that the thickness of the CND can vary with the accretion rate (e.g., Kawakatu & Wada 2008). It should be noted that the Eddington ratio of NGC 1275 ( $\sim 10^{-3}$ ) is close to the boundary between Seyfert AGNs and low-luminosity AGNs, which are thought to have a standard disk and radiatively inefficient accretion flow type accretion flows (Narayan & Yi 1994; Yuan & Narayan 2014), respectively. Thus, the disk thickness of NGC 1275 may be different from that in typical Seyfert AGNs.

In the cosmological context, BCGs provide a unique opportunity to test the scenario of hierarchical galaxy formation along with the cluster formation. BCGs are the most luminous and massive galaxies in the universe at the present epoch and

are typically located near the center of their parent clusters. They are basically interpreted to form through the merger of several massive galaxies in the cluster’s history (Dubinski 1998; De Lucia et al. 2006; Tonini et al. 2012). Galaxy mergers are thought to grow the SMBH and drive the scaling relation between SMBHs and their host galaxies (e.g., Kormendy & Ho 2013; McConnell & Ma 2013). It is therefore natural to expect that the most massive SMBHs reside in BCGs. ALMA can probe molecular gas dynamics within the sphere of gravitational influence (SoI) for the nearby BCGs including NGC 1275, which allows us to measure the SMBH mass.

In this paper, we present ALMA observations of NGC 1275 using the CO(2–1), HCN(3–2), and HCO<sup>+</sup>(3–2) lines to study the cold gas morphology and kinematics from sub-kiloparsec to  $\sim 30$  pc scale. Throughout this paper, we use  $H_0 = 70.5 \text{ km s}^{-1} \text{ Mpc}^{-1}$ ,  $\Omega_M = 0.27$ , and  $\Omega_{\Lambda} = 0.73$ . At the 3C 84 distance,  $0''.1$  corresponds to 34.4 pc.

## 2. Observations and Data Analysis

We proposed ALMA observations to study the morphological and kinematic properties of the cold molecular gas in the circumnuclear region ( $\sim 100$  pc) of NGC 1275 in ALMA Cycle 5, which was approved as the project code 2017.1.01257.S. The proposal consists of two Group Observing Unit Sets (OUSs), one for the observation of the CO(2–1) transition and the other for the observation of the HCN(3–2) and HCO<sup>+</sup>(3–2) transitions. Each Group OUS splits into two Member OUSs, where one is for the observation with an extended configuration (C43-7) and the other is for the observation with a compact configuration (C43-4). This paper presents the results from the observations with the extended configuration.

The observations were made in ALMA Band 6 ( $\lambda = 1.3$  mm) with 47 antennas on 2017 November 27 and 28 for the CO(2–1) and HCN(3–2)/HCO<sup>+</sup>(3–2), respectively. The maximum and minimum baseline lengths are 8.5 km and 92.1 m, respectively. The observations consist of 52 scans for the CO(2–1) and 46 scans for the HCN(3–2)/HCO<sup>+</sup>(3–2) with a 54.4 s integration for each scan bracketed by the scans for the complex gain calibrator observations. Integration time per interferometric visibility was set to 2 s. Table 1 summarizes the observations. Both *X* and *Y* linear polarizations were received and parallel-hand correlations (*XX* and *YY*) were obtained by the ALMA 64-input correlator. For the CO(2–1) observation, two spectral windows (spws) were set in both the lower sideband (LSB) and the upper sideband (USB), with 1920 channels per spw (0.977 MHz channel resolution or  $\sim 1.3 \text{ km s}^{-1}$  velocity resolution) and 64 channels per spw (15.625 MHz channel resolution or  $19.5 \text{ km s}^{-1}$  velocity resolution) for the LSB and USB, respectively. One of the spws in the LSB was centered at a frequency slightly shifted from the expected CO(2–1) frequency so that another spw in the LSB can partially cover the CN(2–1) line.<sup>15</sup> For the HCN(3–2) and HCO<sup>+</sup>(3–2) observations, two spectral windows (spws) were set in both the LSB and the USB, with 64 channels per spw (15.625 MHz channel resolution or  $19 \text{ km s}^{-1}$  velocity resolution) and 1920 channels per spw (0.977 MHz channel resolution or  $\sim 1.1 \text{ km s}^{-1}$  velocity

<sup>15</sup> The CN(2–1) is not detected by our observations. The spectral dynamic range should be similar to that of the CO(2–1) spw. Thus, we can give an upper limit of  $\sim 6.8 \text{ mJy}$  (see Table 3).

**Table 1**  
Observation Summary

Target Lines	ToS (minutes) <sup>a</sup>	NoA <sup>b</sup>	Bandpass <sup>c</sup>	Gain <sup>d</sup>	$T_{\text{sys}}$ <sup>e</sup>	MRS <sup>f</sup>
CO(2–1)	45	47	J0237+2848	J0313+4120	100 K	1''8 (610 pc)
HCN(3–2), HCO <sup>+</sup> (3–2)	39	47	J0237+2848	J0313+4120	120 K	1''5 (530 pc)

**Notes.**<sup>a</sup> Total integration time on NGC 1275.<sup>b</sup> Number of antennas participating in the observation.<sup>c</sup> Bandpass calibrator. Note that the bandpass calibrator is also used as the flux calibrator to derive the amplitude scaling.<sup>d</sup> Complex gain calibrator.<sup>e</sup> Typical system temperature.<sup>f</sup> Maximum recoverable scale given by  $0.6\lambda/D_{\text{min}}$  (see Warmels et al. 2018), where  $D_{\text{min}}$  is the minimum baseline length.

resolution) for the LSB and USB, respectively. One spw in the USB was centered at the HCN(3–2) line and one at the HCO<sup>+</sup>(3–2) line.

The data were processed at EA-ARC with the CASA 5.1.1-5 and ALMA Pipeline version 40896. Amplitude calibration was performed using measurements of the system temperature ( $T_{\text{sys}}$ ) on a channel-by-channel basis. Rapid phase variations on timescales of less than the gain calibration cycle were corrected using the water vapor radiometer (WVR). Unreliable data such as amplitude phase jumps and low antenna gains were automatically identified by the ALMA Pipeline and flagged. The bandpass calibration was done in both phase and amplitude. Temporal variation of the gain amplitude and phase was calibrated using the averaged  $XX$  and  $YY$  correlations of a gain calibrator. Flux scaling was derived on the bandpass calibrator using the flux information provided by the Joint ALMA Observatory (JAO). The referenced flux was derived with the interpolation (power-law spectral index of  $-0.63$ ) from measurements in Bands 3 and 7 on 2017 November 27.

After applying all calibrations, it was found that the pipeline calibration was not sufficient to correct the phase delay, which was seen in both gain calibrator and NGC 1275. The residual delay was antenna-dependent and time-variable from scan to scan, which showed variations within at most  $\pm 20$  ps. This amount of delay can cause a phase slope of a few degrees across one spw. Thanks to bright continuum emission from NGC 1275 ( $\sim 7$  Jy), we calibrated the residual delay using the CASA task `gaincal` with `gaintype = K`. Since NGC 1275 can be observed at low elevation from the ALMA site, the visibility phase showed very rapid time variation, which cannot be fully corrected with the usual gain calibration or WVR correction. Thus, we performed self-calibration using the continuum emission of NGC 1275 in both phase and amplitude. The phase and amplitude self-calibration were done per integration time and per scan, respectively.

The continuum emission was identified in line-free channels with a fitting order of one using the CASA task `uvcontsub`. Images were created with a velocity resolution of  $20 \text{ km s}^{-1}$  with the “nearest” interpolation in frequency. Deconvolution was done with the CLEAN algorithm using the CASA task `tclean` non-interactively. In the following sections, we show images with both natural weighting and Briggs weighting (Briggs 1995) of robust parameter 0.5. The beam shapes for all images are summarized in Table 2. Those for archival data (see Section 3.2) are also summarized in the same table.

We note that some residual emissions at the image center are seen in the line-free channels even after the continuum subtraction. Those emissions are not constant over the channels but appear almost randomly from channel to channel. This is

**Table 2**  
Beam Shape

Target Lines	Natural <sup>a</sup>	Briggs <sup>b</sup>
CO(2–1)	$0''.144 \times 0''.077$ at $4^\circ 0'$	$0''.110 \times 0''.048$ at $0^\circ$
HCN(3–2)	$0''.129 \times 0''.076$ at $12^\circ 1'$	$0''.098 \times 0''.045$ at $9^\circ 4'$
HCO <sup>+</sup> (3–2)	$0''.129 \times 0''.076$ at $12^\circ 0'$	$0''.099 \times 0''.045$ at $9^\circ 3'$
HCN(3–2) (archival data)	... <sup>c</sup>	$0''.901 \times 0''.363$ at $-0^\circ 5'$
HCO <sup>+</sup> (3–2) (archival data)	... <sup>c</sup>	$0''.919 \times 0''.371$ at $0^\circ 5'$

**Notes.**<sup>a</sup> The beam shape for the images with natural weighting.<sup>b</sup> The beam shape for the images with Briggs weighting (robust = 0.5).<sup>c</sup> We use only the images with Briggs weighting for the spectral measurement of archival data.

most likely due to the limitation of spectral dynamic range caused by the uncertainty in bandpass calibration. Assuming that the bandpass accuracy depends on the signal-to-noise ratio of the bandpass calibrator and that the residual after the bandpass calibration is random over antennas and frequency, we can estimate the spectral dynamic range  $D_{\text{spec}}$  as  $D_{\text{spec}} = I_{\text{BP}}/\sigma_{\text{BP}}$  where  $I_{\text{BP}}$  is the flux density of the bandpass calibrator and  $\sigma_{\text{BP}}$  is the sensitivity for the bandpass calibrator scan. We estimate  $\sigma_{\text{BP}}$  using the measured image rms on the bandpass calibrator image. The image of the target source should also exhibit an error given by  $\sigma_{\text{T}} = I_{\text{T}}/D_{\text{spec}}$  after the continuum subtraction, where  $I_{\text{T}}$  is the continuum flux density of the target source. Table 3 summarizes the values of these parameters. The estimated spectral dynamic range is nearly consistent with the demonstrated spectral dynamic range of 1000 given in the ALMA Proposer’s Guide and Technical Handbook (Andreani et al. 2018; Warmels et al. 2018). Using the measured continuum emission for  $I_{\text{T}}$ , we obtain uncertainties ( $\sigma_{\text{T}}$ ) of 6.8 mJy, 5.5 mJy, and 6.3 mJy for the CO(2–1), HCN(3–2), and HCO<sup>+</sup>(3–2) lines, respectively. These uncertainties dominate the off-position image rms of  $\sim 1$  mJy (see Section 3). In the following sections, we will show the observed spectra integrated over the circular apertures of  $0''.8$  and  $0''.3$  diameter. We propagate the above uncertainties into our analysis for the spectra. We obtain  $\sigma_{\text{T}}$  of 4.3 mJy for both HCN(3–2) and HCO<sup>+</sup>(3–2) for the archival data (see Section 3.2). The reason for a better  $\sigma_{\text{T}}$  in the archival data is that the data were taken in relatively good weather conditions in terms of  $T_{\text{sys}}$  and WVR, and the bandpass calibrator is brighter so that it provides a better signal-to-noise ratio for the bandpass calibration. For an additional validation, we measured

**Table 3**  
Spectral Dynamic Range

Target Lines	$\nu_{\text{rest}}$ (GHz) <sup>a</sup>	$I_{\text{BP}}$ (Jy) <sup>b</sup>	$\sigma_{\text{BP}}$ (mJy) <sup>c</sup>	$D_{\text{spec}}$ <sup>d</sup>	$I_{\text{T}}$ (Jy) <sup>e</sup>	$\sigma_{\text{T}}$ (mJy) <sup>f</sup>
CO(2–1)	230.538	1.082	1.03	1050	7.15	6.81
HCN(3–2)	265.886	0.989	0.76	1301	7.14	5.49
HCO <sup>+</sup> (3–2)	267.558	0.985	0.87	1132	7.13	6.30
HCN(3–2) (archival data)	265.886	1.595	0.75	2141	9.26	4.33
HCO <sup>+</sup> (3–2) (archival data)	267.558	1.590	0.75	2134	9.26	4.34

**Notes.**

<sup>a</sup> Rest frequency of the line.

<sup>b</sup> Flux density of bandpass calibrator (J0237+2848).

<sup>c</sup>  $1\sigma$  sensitivity for bandpass calibrator (J0237+2848) scan.

<sup>d</sup> Spectral dynamic range.

<sup>e</sup> Flux density of target source (NGC 1275).

<sup>f</sup> Expected error for target source (NGC 1275).

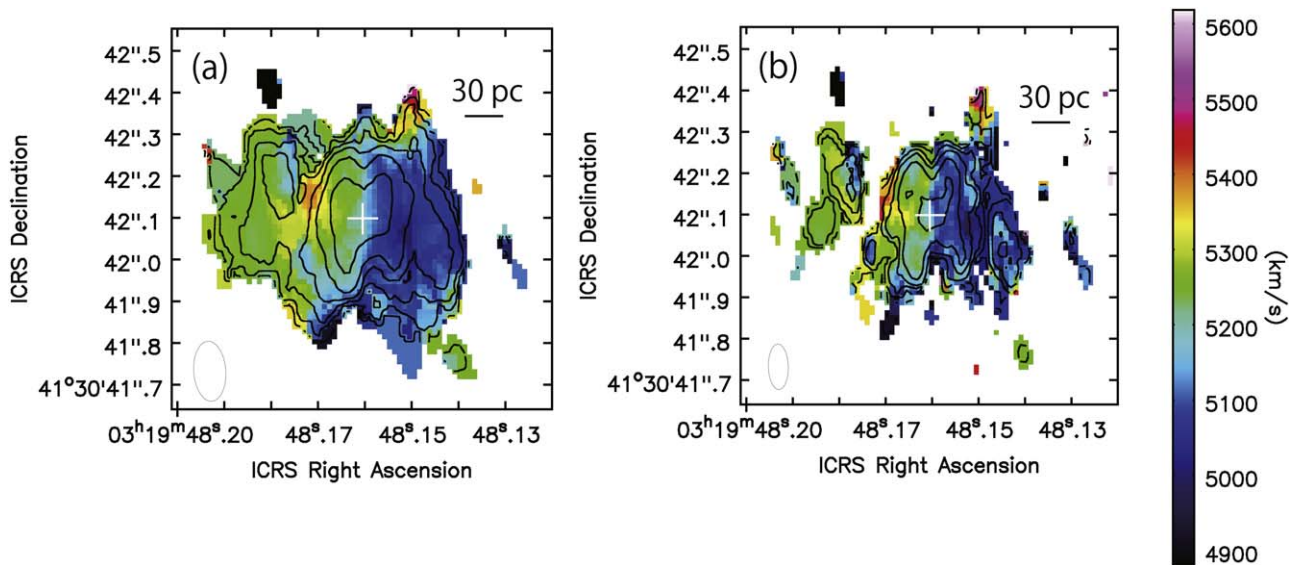


**Figure 1.** (a) Contours of the naturally weighted moment 0 map overlaid on the colored moment 1 map of CO(2–1). The cross symbol indicates the AGN position, which was identified as the peak position of the continuum emission. (b) The same as (a), but the image is created using the Briggs weighting with the robust parameter of 0.5. The images are plotted throughout the region where the flux density is greater than  $5\sigma$  ( $1\sigma = 0.87$  mJy for the naturally weighted image and  $1\sigma = 0.79$  mJy for the Briggs weighted image). The contours are plotted at the level of  $20 \text{ km s}^{-1} \times 3\sigma \times (-1, 1, 2, 4, \dots, 512)$ . The image rms is measured within a circle of radius of  $1''.8$  (150 pixels) at the image center in line-free channels (averaged over 30 channels around  $6000 \text{ km s}^{-1}$ ). The beam size is  $0''.144 \times 0''.077$  at the position angle of  $4^\circ$  and  $0''.110 \times 0''.048$  at the position angle of  $0^\circ$  for natural weighting and Briggs weighting, respectively.

the image rms within the same aperture used for Figure 3 after the continuum subtraction for the line-free spws. The measured rms is about 0.9 mJy, which is smaller than  $\sigma_{\text{T}}$ . Thus, we confirmed that the baseline oscillation in line-free spws does not exceed the estimated uncertainties.

### 3. Results

#### 3.1. The CO(2–1) Line

Figure 1(a) shows the contours of a naturally weighted velocity-integrated map (moment 0 map) overlaid on the velocity-weighted intensity map (moment 1 map) of the CO(2–1) line. The emissions are mostly detected within a radius of 100 pc. The structure seems to show a disk-like morphology. We can see a clear velocity gradient of about  $\pm 250 \text{ km s}^{-1}$  at a position angle of  $\sim 70^\circ$  (Figure 2). The intensity-weighted velocity at the AGN position is about  $5200 \text{ km s}^{-1}$ , which is consistent with the optical systemic velocity. The velocity gradient likely originates in the

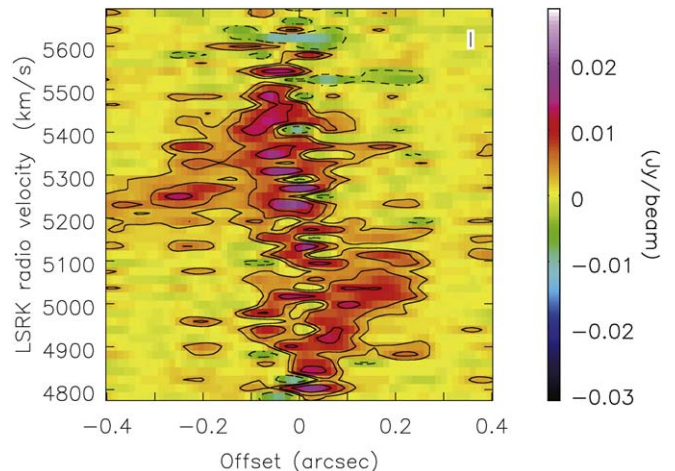


**Figure 2.** Position–velocity diagram of CO(2–1) along the axis passing through the image center of Figure 1 at a position angle of  $70^\circ$ .

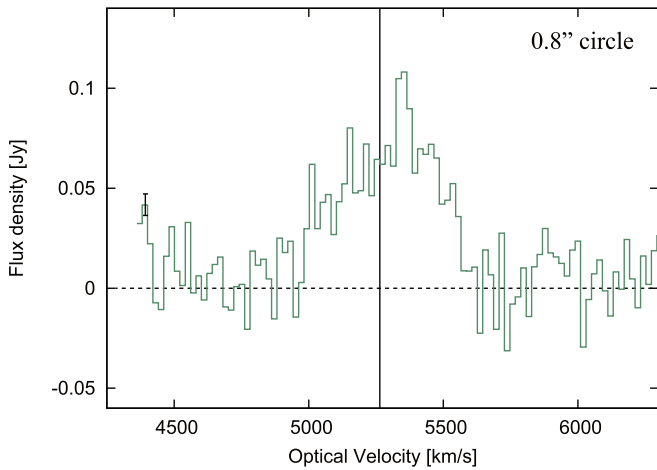


**Figure 3.** Integrated spectrum of CO(2–1) over a circular region of  $0.8''$  diameter at the galaxy center. An error bar corresponding to  $\pm 1\sigma$  uncertainty (6.8 mJy) is plotted in the panel. The error estimation is explained in the text (see Section 2). The vertical line indicates the systemic velocity of NGC 1275.

rotational motion of the gas disk, which is also evident in the HCN(3–2) and  $\text{HCO}^+(3-2)$  emissions (see next subsection). The integrated spectrum over the central  $0.8''$  is shown in Figure 3. The emission is centered nearly at the systemic velocity, ranging from  $\sim 5000 \text{ km s}^{-1}$  ( $v - v_{\text{sys}} \simeq -264 \text{ km s}^{-1}$ ) to  $\sim 5600 \text{ km s}^{-1}$  ( $v - v_{\text{sys}} \simeq 336 \text{ km s}^{-1}$ ). Previous Gemini observations of the warm  $\text{H}_2$  gas (Scharwächter et al. 2013) revealed a similar rotating disk structure within a radius of  $\sim 0.15''$  ( $\sim 50 \text{ pc}$ ). The line width of the warm  $\text{H}_2$  gas shows an FWHM of  $\sim 350 \text{ km s}^{-1}$ . Both morphological and kinematic structures of CO(2–1) as well as its spectral shape are quite consistent with those for the warm  $\text{H}_2$  gas, but our observed disk seems to have clumpy or filamentary substructures (see the image with higher angular resolution created using the Briggs weighting with the robust parameter of 0.5, Figure 1(b)). The CO counterpart of the  $\text{H}_2$  gas stream, southwest from the center (Scharwächter et al. 2013), is not detected in our images. We note that there should be missing flux of an extended structure in our data because of the lack of short interferometric baselines, so the whole structure of the disk can be larger. The peak flux ( $\sim 0.1 \text{ Jy}$ ) of the integrated spectrum (Figure 3) is about half of that of the “inner filament” (see Figure 4(a)) presented in Lim et al. (2008). The peak of the spectrum is at  $5340 \text{ km s}^{-1}$ , which is about  $100 \text{ km s}^{-1}$  redshifted from the systemic velocity, while the spectral shape of the inner filament in Lim et al. (2008) is rather symmetric and centered at the systemic velocity. This indicates that the blueshifted emission is resolved even more strongly in our observations.

Some extended features are marginally detected in the western region in the naturally weighted image (Figure 4). Three components (denoted A, B, and C in Figure 4(b)) are mainly detected at  $\sim 8''$ ,  $\sim 5''$ , and  $\sim 2''$  from the center at a position angle of  $-80^\circ$  at  $v \sim 5091 \text{ km s}^{-1}$  ( $v - v_{\text{sys}} \simeq -173 \text{ km s}^{-1}$ ). Those components probably represent dense, compact regions within the filaments reported by Lim et al. (2008). One of the outer components (A) was identified as a prominent knot-like feature with relative velocity of  $\sim -150 \text{ km s}^{-1}$  in the western filament in Lim et al. (2008). The inner components (B and C) seems to constitute the western elongation of the inner filament. Another features (denoted D in Figure 4(c)) is marginally detected at  $\sim 4''$ – $5''$  from the center at a position angle of  $-90^\circ$  at  $v \sim 5211 \text{ km s}^{-1}$  ( $v - v_{\text{sys}} \simeq -53 \text{ km s}^{-1}$ ).

A part of the feature is also detected at  $v \sim 5251 \text{ km s}^{-1}$  ( $v - v_{\text{sys}} \simeq -13 \text{ km s}^{-1}$ , denoted E in Figure 4(d)). No emission, except for the main disk emission, is detected in other velocity channels. All the features from  $v \sim 5091 \text{ km s}^{-1}$  to  $v \sim 5251 \text{ km s}^{-1}$  seem to be hardly reproduced by a single stream of infalling gas since the components are not all aligned at the same position angle. Lim et al. (2008) also pointed out that the inner filament and the western filament are separate structures because of their different kinematic structures, and we confirmed this in our high-resolution images.

### 3.2. The HCN(3–2) and $\text{HCO}^+(3-2)$ Lines

Figures 5(a) and 6(a) show the contours of naturally weighted moment 0 maps overlaid on the moment 1 maps of HCN(3–2) and  $\text{HCO}^+(3-2)$ , respectively. The images created with the Briggs weighting are also shown in Figures 5(b) and 6(b). These emissions are detected only within a radius of 100 pc, and the morphological and kinematic structures are also similar to those of the CO(2–1) emission. Those molecules also show a velocity gradient, as seen in the CO(2–1) emission. Figure 7(a) shows the spectrum integrated over the central  $0.8''$ . Those spectral shapes are similar to the CO(2–1) spectrum, which is peaked at  $\sim 5330 \text{ km s}^{-1}$  and ranges from 5000 to 5600  $\text{km s}^{-1}$ . Previous single-dish observations showed a consistent line width and line peak (Salomé et al. 2008; Bayet et al. 2011).

One notable finding is that absorption features are detected at velocities of  $\sim 4600$ – $4900 \text{ km s}^{-1}$  (Figure 7). The significance is more than  $3\sigma$  and  $4\sigma$  in the deepest absorption channels for HCN(3–2) and  $\text{HCO}^+(3-2)$ , respectively. Since there are no corresponding major transitions of molecules at these frequencies, those features are most likely the blueshifted components of the HCN(3–2) and  $\text{HCO}^+(3-2)$  lines shifted by 300–600  $\text{km s}^{-1}$  with respect to the systemic velocity. Figure 8 shows an example of a channel map where the absorption is detected. This indicates that the absorption occurs in the direction to the central bright continuum associated with the AGN jet. The flux density of the background continuum emission is about  $7 \text{ Jy beam}^{-1}$  while the peak flux of the absorption features is about  $40 \text{ mJy beam}^{-1}$ , yielding an optical depth of 0.0057. Under the assumption of local thermodynamic equilibrium and a covering factor of 1, we obtain an  $\text{H}_2$  column density of  $2.3 \times 10^{22} \text{ cm}^{-2}$ . Here we assume an HCN/ $\text{H}_2$  abundance ratio of  $10^{-9}$  (Smith & Wardle 2014). To check that these features are not an artifact caused by the process of continuum subtraction, we also show the spectrum measured on the continuum-unsubtracted images in Figure 9. Troughs in the spectrum are clearly seen between 261.6 GHz and 261.9 GHz for HCN(3–2) and between 263.2 GHz and 263.7 GHz for  $\text{HCO}^+(3-2)$ .

To confirm the detection of absorption features, we also reduced archival data for which NGC 1275 was observed as the phase calibrator (Project ID: 2013.1.01102.S). These data covered the frequencies of the HCN(3–2) and  $\text{HCO}^+(3-2)$  lines. Figure 10(b) shows the spectra of those lines. Absorptions in the spectra could be marginally detected at a velocity of  $\sim 4620$ – $4900 \text{ km s}^{-1}$  with a significance of at most  $3\sigma$  for HCN(3–2) and  $2\sigma$  for  $\text{HCO}^+(3-2)$  in the deepest absorption channels. Low significance might be due to a relatively large beam size for the archival data. However, we note that the marginal detection does not conflict with the detection with our

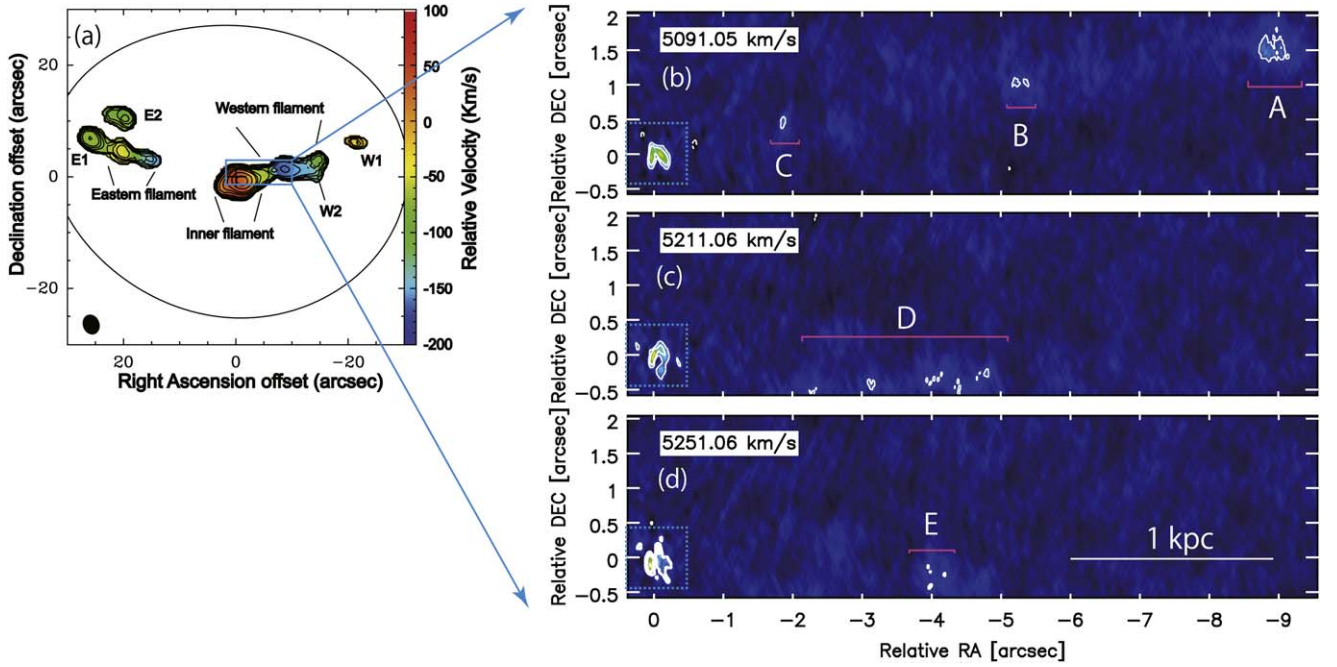


**Figure 4.** (a) Contours of the moment 0 map overlaid on the colored moment 1 map from previous Submillimeter Array observations (Lim et al. 2008). (b)–(d) Large-scale channel maps of the CO(2–1) intensity from our ALMA observations at  $v = 5091 \text{ km s}^{-1}$  ( $v - v_{\text{sys}} = -173 \text{ km s}^{-1}$ ),  $5211 \text{ km s}^{-1}$  ( $v - v_{\text{sys}} = -53 \text{ km s}^{-1}$ ), and  $5251 \text{ km s}^{-1}$  ( $v - v_{\text{sys}} = -13 \text{ km s}^{-1}$ ). The images were created with natural weighting. The contours are plotted at  $5\sigma \times (-1, 1, 2, 4, \dots, 32)$ , where  $1\sigma = 0.87 \text{ mJy}$ . The locations where the large-scale emissions are detected are highlighted by the magenta lines. The rectangle shown by cyan lines in (a) indicates the region where the ALMA images are shown in (b)–(d). The rectangle shown by broken cyan lines in (b)–(d) corresponds to the region shown in Figure 1.

data because of a possible time variation of the properties of absorbers. We will discuss this in detail in Section 4.3.

## 4. Discussion

### 4.1. Filaments

Our ALMA observations detected two distinct filamentary structures—one is seen at  $\sim 5091 \text{ km s}^{-1}$  at a position angle of  $\sim -80^\circ$  (A, B, and C in Figure 4) and the other at  $v \sim 5211\text{--}5251 \text{ km s}^{-1}$  at a position angle of  $\sim -90^\circ$  (D and E in Figure 4). Each component has a total  $\text{H}_2$  gas mass of  $\sim 10^6 M_\odot$  (the assumptions used for this estimate are discussed in Section 4.2). Note that the estimated mass should be a lower limit since the total emissions cannot be recovered because of the lack of short interferometric baselines. Components with lower velocity mainly constitute the western filament while those with higher velocity constitute the inner filament. Previous authors argued that the large-scale gas filaments can be infalling and settling into the CND (e.g., Scharwächter et al. 2013). However, these features may not be a representation of a single infalling stream since they are not simply connected to each other in terms of both morphology and kinematics. We have not so far detected direct evidence of the connection between the filaments and the CND.

Yet the complex filaments in NGC 1275 can be a natural consequence of CCA enhanced by thermal instabilities. Numerical simulations of elliptical galaxies suggest that the growth of thermal instabilities in the hot halo/cluster gas leads to the condensation of cold clouds and filaments (Gaspari et al. 2013, 2017). As a result, the accretion flow from cluster scales to the central black hole is dominated by CCA, i.e., the cold clouds show complex structures and non-ballistic orbits (Pizzolato & Soker 2010; Gaspari et al. 2013, 2017). The observed complex morphology of the CO filaments seems to be

consistent with the simulations. As we noted in Section 1, deflection of jets and strong variation in the AGN luminosity of NGC 1275 are observed. This is also consistent with the predictions of CCA. Our observations may not be sufficient to reconstruct the entire gas structures because of the lack of short interferometric baselines. Observations with a compact antenna configuration would aid in imaging more diffuse and extended structures.

How much of the cold gas is accreted by the SMBH? We can make a crude estimate if cold accretion is the dominant feeding mechanism for the NGC 1275 system. Assuming each component is infalling to the center, we can roughly estimate the mass accretion rate as

$$\begin{aligned} \dot{M}_{\text{cold}} &= \frac{M_{\text{cold}}}{t_{\text{dyn}}} = M_{\text{cold}} \left( \frac{r}{v} \right)^{-1} \\ &= 0.1 \times \left[ \frac{M_{\text{cold}}}{10^6 M_\odot} \right] \left[ \frac{r}{1 \text{ kpc}} \right]^{-1} \left[ \frac{v}{100 \text{ km s}^{-1}} \right] M_\odot \text{ yr}^{-1}. \end{aligned} \quad (1)$$

Here  $M_{\text{cold}}$  is the cold gas mass,  $v$  is the infalling velocity, and  $r$  is the distance to each clump from the AGN. For the first-order approximation, we assume that three-dimensional velocity of each component is similar to the observed line-of-sight velocity. As an example, the most pronounced component (component A in Figure 4(b)) has a velocity of  $\sim 170 \text{ km s}^{-1}$  relative to the systemic velocity. Each of components A–E in Figure 4 has an  $\text{H}_2$  gas mass of  $\sim 10^6 M_\odot$  (see Section 4.2 about the details of conversion from the observed flux density to gas mass). Taking into account that the estimated gas mass is a lower limit because of missing flux, we obtain  $\dot{M} > 0.1 M_\odot \text{ yr}^{-1}$ . Similar estimates were made by Lim et al. (2008), and they obtained a mass

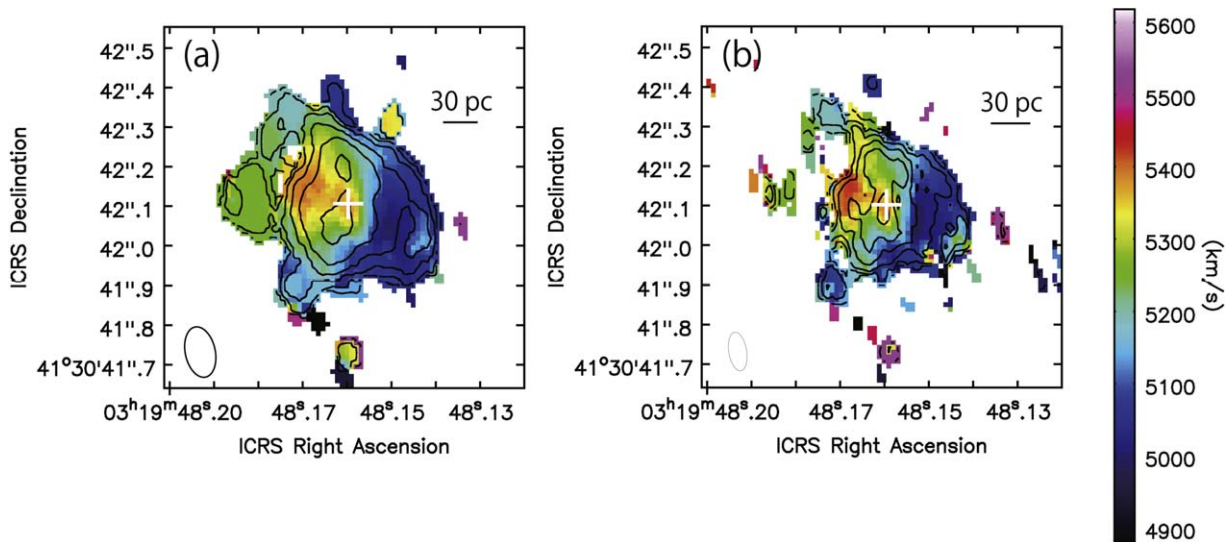


**Figure 5.** (a) Contours of the naturally weighted moment 0 map overlaid on the colored moment 1 map of HCN(3–2), which was identified as the peak position of the continuum emission. (b) The same as (a), but the image is created using the Briggs weighting with the robust parameter of 0.5. The images are plotted for the region where the flux density is greater than  $5\sigma$  ( $1\sigma = 0.95$  mJy for the naturally weighted image and  $1\sigma = 0.84$  mJy for the Briggs weighted image). The contours are plotted at the level of  $20 \text{ km s}^{-1} \times 3\sigma \times (-1, 1, 2, 4, \dots, 512)$ . The image rms is measured within a circle of radius of  $1''.8$  (150 pixels) at the image center in line-free channels (averaged over 30 channels around  $6000 \text{ km s}^{-1}$ ). The beam size is  $0''.129 \times 0''.076$  at the position angle of  $12^\circ.1$  and  $0''.098 \times 0''.045$  at the position angle of  $9^\circ.4$  for natural weighting and Briggs weighting, respectively.

accretion rate of several tens of solar masses per year. Thus, our estimate does not conflict with the estimate by Lim et al. (2008). Fujita et al. (2016) estimated the Bondi power of NGC 1275 using *Chandra* X-ray observations of the hot gas and the argument of momentum balance between the jet/cocoon and the ambient medium. The resultant Bondi accretion rate was  $7.4 \times 10^{-5} M_\odot \text{ yr}^{-1}$  considering current jet activities (see Fujita et al. 2016 for more details). This suggests that the cold accretion can be more efficient than hot accretion on the kiloparsec scale of NGC 1275.

#### 4.2. Inner Gas Disk

A rotating disk-like morphology and kinematics are detected in the CO(2–1), HCN(3–2), and HCO<sup>+</sup>(3–2) lines. The gas disk spatially coincides with the warm H<sub>2</sub> gas disk (Scharwächter et al. 2013), and the velocity structure is also very similar between the two data sets. Although our data alone cannot give a robust constraint on the gas temperature, the temperature of the CNB traced by the cold molecular lines (CO(2–1), HCN(3–2), and HCO<sup>+</sup>(3–2)) is probably less than 100 K (e.g., Myers 1978). On the other hand, H<sub>2</sub> emission can trace gas with a temperature greater than 1000 K (Wilman et al. 2005; Scharwächter et al. 2013). Therefore, it is natural to expect that the cold and warm gas phases are distributed at the same radii but are stratified. This multiphase gas structure can be realized if the gas disk consists of many small gas clumps where the temperature of the outer surface of clumps is raised by shocks or UV and X-ray irradiation so that the H<sub>2</sub> molecules can be collisionally excited while the inner part remains at a low temperature and is where the cold molecular lines are emitted. Such a multiphase gas system is also predicted by the CCA simulations (Gaspari et al. 2017).

We calculate the total H<sub>2</sub> gas mass using Equations (3) and (4) in Solomon & Vanden Bout (2005) and obtain  $\sim 4 \times 10^8 M_\odot$ . Here we get the CO(2–1) integrated flux density of  $40 \text{ Jy km s}^{-1}$  within the central  $1''$  with a velocity FWHM of

$400 \text{ km s}^{-1}$ . We assumed a ratio of CO(2–1) to CO(1–0) of one and the conversion factor from CO luminosity to H<sub>2</sub> mass to be that in our Galaxy ( $\alpha_{\text{CO}} = 4.6 M_\odot \text{ pc}^{-2} (\text{K km s}^{-1})^{-1}$ ) (Solomon & Vanden Bout 2005). The derived gas mass is about 20% of the total gas mass of the inner filament presented in Lim et al. (2008). If we use  $\alpha_{\text{CO}} = 0.6\text{--}0.8$ , which is widely used as the conversion factor for gas-rich galaxies at high redshift and local ultra-luminous/luminous infrared galaxies (Downes & Solomon 1998; Papadopoulos et al. 2012), we obtain a total gas mass of  $\sim (5\text{--}7) \times 10^7 M_\odot$ . Izumi et al. (2016) reported a correlation between the mass of cold molecular gas ( $M_{\text{gas}}$ ) in the CND and the black hole accretion rate  $\dot{M}$  for Seyfert galaxies. Using the derived correlation and  $M_{\text{gas}} = 4 \times 10^8 M_\odot$ , we obtain  $\dot{M}_{\text{BH}}$  of  $\sim 5 \times 10^{-2} M_\odot \text{ yr}^{-1}$ , which agrees with the accretion rate ( $\sim 1 \times 10^{-1} M_\odot \text{ yr}^{-1}$ ) inferred from the bolometric luminosity (Nagai et al. 2017) within a factor of two.

The CCA simulations predict that the evolution of condensation in a quiescent rotating hot halo leads to the formation of a multiphase disk (Gaspari et al. 2017). In the equatorial plane ( $x$ – $y$  plane), the infalling gas spins-up increasing its rotational velocity to conserve its initial angular momentum. The gas also gradually goes into freefall along the  $z$  direction (perpendicular to the equatorial plane). This drives the gas motion to follow a conical helix, but after a long duration (40 Myr in Gaspari et al. 2017) the angular momentum in  $x$  and  $y$  directions is canceled out by cloud–cloud collisions and the multiphase gas converges to the equatorial disk. Low gas density along the jet direction is indeed suggested by VLBI observations (Fujita et al. 2016; Fujita & Nagai 2017). Both the cold gas disk (CO(2–1), HCN(3–2), and HCO<sup>+</sup>(3–2)) and the warm H<sub>2</sub> disk extend to a radius of  $\sim 0''.3$  ( $\sim 100 \text{ pc}$ ). We can conclude that the rotational motion dominates the turbulent motion at  $\sim 100 \text{ pc}$  in terms of the CCA. Gaspari et al. (2017) reported that the dense disk blocks the inflow of gas at a large distance from the center, leading to the expansion of the disk radius with time. Larger cold gas disks, extending to a few kiloparsecs, were found in many other early-type galaxies by

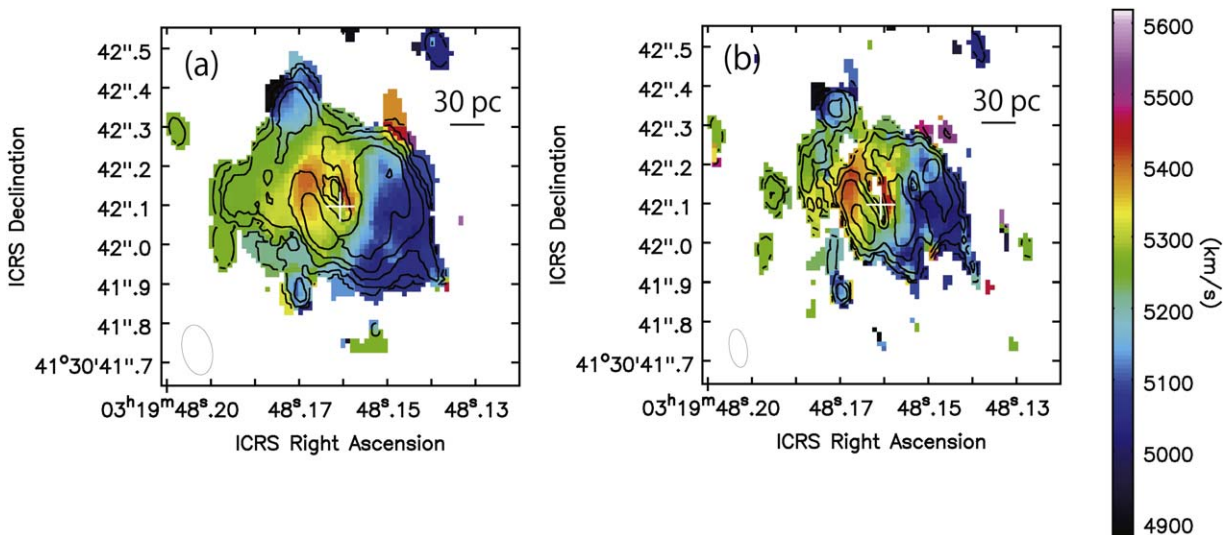


**Figure 6.** (a) Contours of the naturally weighted moment 0 map overlaid on the colored moment 1 map of HCO<sup>+</sup>(3–2). The cross symbol indicates the AGN position, which was identified as the peak position of the continuum emission. (b) The same as (a), but the image is created using the Briggs weighting with the robust parameter of 0.5. The images are plotted for the region where the flux density is greater than  $5\sigma$  ( $1\sigma = 1.05$  mJy for the naturally weighted image and  $1\sigma = 0.96$  mJy for the Briggs weighted image). The contours are plotted at the level of  $20 \text{ km s}^{-1} \times 3\sigma \times (-1, 1, 2, 4, \dots, 512)$ . The image rms is measured within a circle of radius of  $1''.8$  (150 pixels) at the image center in line-free channels (averaged over 30 channels around  $6000 \text{ km s}^{-1}$ ). The beam size is  $0''.129 \times 0''.076$  at the position angle of  $12^\circ 0$  and  $0''.099 \times 0''.045$  at the position angle of  $9^\circ 3$  for natural weighting and Briggs weighting, respectively.

the CARMA CO(1–0) imaging survey of early-type galaxies (Alatalo et al. 2013) and in radio galaxies by ALMA CO(2–1) (Ruffa et al. 2019). Compared to those early-type galaxies or radio galaxies, the gas disk in NGC 1275 is remarkably small. This might be explained by relatively strong jet activity. NGC 1275 has repeated strong AGN outbursts, and thus the jet/cocoon in the polar region could have uplifted the gas and stirred up the turbulence (Churazov et al. 2001; Enßlin & Vogt 2006). This can suppress gas infall from the hot atmosphere. The extended emission line nebula around NGC 1275 (Hatch et al. 2006; Fabian et al. 2008; Gendron-Marsolais et al. 2018) could be a signature of such gas uplifted by radio jets/bubbles. All galaxies in Alatalo et al. (2013) show much lower radio continuum flux than NGC 1275, so the jet feedback can be less efficient for those galaxies. This scenario also supports the lack of kiloparsec-scale gas disks in PKS 0745–191 (Russell et al. 2016), Phoenix cluster (Russell et al. 2017), and A2597 (Tremblay et al. 2016), which all show strong jet activities. Recently, the disk around the nucleus of the powerful radio galaxy Cygnus A has been also imaged by the observation of free–free emission (Carilli et al. 2019). This observation also shows a relatively compact ( $500 \text{ pc} \times 300 \text{ pc}$ ) disk. In contrast, the radio galaxies Hydra A and 3C 31 have kiloparsec-scale molecular gas/dust disks (Okuda et al. 2005; Fujita et al. 2013; Hamer et al. 2014). In particular, Hydra A shares many properties, including the strong jet activity, with NGC 1275 (Hamer et al. 2014). The existence of a cold gas disk on kiloparsec scales in Hydra A may suggest that the cluster gas is less turbulent for some reason, so the CCA cannot develop. Low turbulence is also indicated by low velocity dispersion of the CO(2–1) gas revealed by the ALMA observations (Rose et al. 2019). The future X-ray satellite mission *XRISM* would help to uncover the gas motion of BCGs in more detail.

A velocity gradient of the gas is observed at a position angle of  $\sim 70^\circ$ . This rotation axis is nearly parallel to the innermost jet axis, which was revealed by the space VLBI observation with RadioAstron (Giovannini et al. 2018). Hiura et al. (2018)

reported the nonlinear jet/hotspot motion on a parsec scale and discussed the possibility that the nonlinear motion was caused by the precession of the jet base. Nevertheless, the precession angle is only a few degrees. Thus, the disk rotation axis is still approximately consistent with the jet axis. The coincidence of the disk and jet axis alignment probably indicates that the molecular gas disk is connected to the inner accretion disk, which is responsible for the jet launching. Alternatively, this might indicate that the spin axis of the central SMBH is aligned to the molecular gas disk if the Blandford–Znajek mechanism (Blandford & Znajek 1977) is responsible for the jet production.

Let us estimate the accretion timescale of the molecular gas in the observed disk. If we assume that the cold gas disk is thin and the kinetic viscosity is the main source of angular momentum transfer, the accretion timescale ( $\tau$ ) can be given by  $\tau = r^2/(\alpha c_s h) = r^2/(vh)$  (e.g., Shakura & Sunyaev 1973; Pringle 1981), where  $r$  is the disk radius,  $\alpha$  is the viscosity parameter,  $c_s$  is the sound speed,  $v$  is the turbulent velocity, and  $h$  is the scale height. Assuming a thin disk ( $h = 0.1r$ ), we get

$$\tau \sim 4 \times 10^7 \times \left[ \frac{r}{100 \text{ pc}} \right] \left[ \frac{v}{25 \text{ km s}^{-1}} \right]^{-1} \text{ yr}. \quad (2)$$

Here we adopt the observed typical dispersion (see Figure 11) for the turbulent velocity ( $v$ ). We should notice that the velocity dispersion at the inner part of CND in Figure 11 does not reflect true turbulent velocity. An apparent large velocity dispersion ( $> 100 \text{ km s}^{-1}$ ) is probably an artifact that is caused by convolving the synthesized beam to a large velocity gradient (see  $-0''.05 \leq x \leq 0''.05$  in Figure 2). We therefore adopt a typical velocity dispersion in the outer region ( $v \sim 25 \text{ km s}^{-1}$ ). We can roughly estimate the averaged accretion rate ( $\dot{M}_{\text{gas}}$ ) of the gas disk within a radius of 100 pc as  $\dot{M}_{\text{gas}} \simeq M_{\text{gas}}/\tau$ . For  $M_{\text{gas}} = (5\text{--}7) \times 10^7 M_\odot$  and  $M_{\text{gas}} = 4 \times 10^8 M_\odot$  (see Section 4.2), we get  $\dot{M}_{\text{gas}} = 1\text{--}2 M_\odot \text{ yr}^{-1}$  and  $\dot{M}_{\text{gas}} = 10 M_\odot \text{ yr}^{-1}$ , respectively. This accretion rate of cold gas is again higher than the Bondi



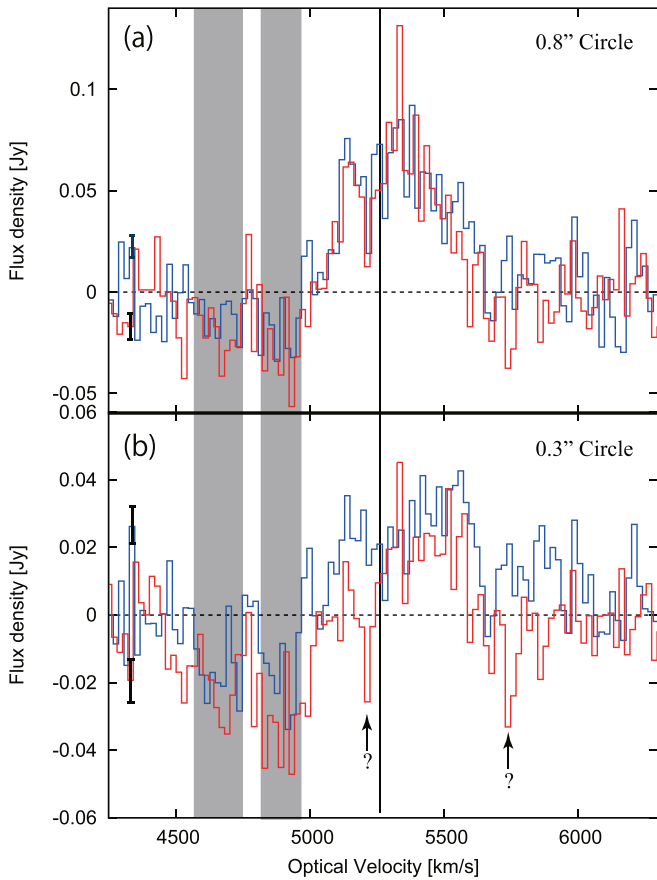


**Figure 7.** (a) The HCN(3–2) (blue) and HCO<sup>+</sup>(3–2) (red) spectra integrated over a circular region of 0<sup>''</sup>.8 diameter at the center. (b) The same as (a), but the spectrum is computed over a circular region of 0<sup>''</sup>.3 diameter at the center. Error bars corresponding to  $\pm 1\sigma$  uncertainty are plotted in each panel (5.5 mJy for HCN(3–2) and 6.3 mJy for HCO<sup>+</sup>(3–2)). The error estimation is explained in the text (see Section 2). The vertical line indicates the systemic optical velocity of 5264 km s<sup>−1</sup>. The velocity ranges where the absorption features are detected most significantly in both HCN(3–2) and HCO<sup>+</sup>(3–2) are highlighted by gray rectangles. Additional deficits are seen in the HCO<sup>+</sup>(3–2) spectrum, as indicated by arrows, but there are no corresponding deficits in the HCN(3–2) spectrum.

accretion rate of  $7.4 \times 10^{-5} M_{\odot}$  (Fujita et al. 2016). This indicates that cold accretion is the dominant channel on the scale of tens of parsecs.

Comparison between the accretion timescale and cooling timescale of the hot ICM would give a hint for the timescale of AGN activity. Sanders et al. (2004) showed the cooling time of hot gas in NGC 1275 at radii down to 5 kpc. Within 10 kpc, the cooling time is estimated to be  $5 \times 10^8$  yr and it does not change very much as a function of distance. The density profile of BCGs is well represented by a  $\beta$ -model with a flat density profile within the core radius. The flat density profile is favored even in the inner region ( $r \sim 100$  pc) of NGC 1275 (Fujita et al. 2016). Since the cooling time is inversely proportional to the density, it should be reasonable to assume that the cooling timescale does not change much within the core radius. Here we use a cooling time of  $10^8$  yr on a scale of 100 pc. This is longer than the accretion timescale. If the angular momentum of the black hole accretion disk is controlled by the cold gas of the CND, the jet-launching direction can also be controlled by the global angular momentum of the CND. We therefore expect that the jet direction would remain more or less the same on the

accretion timescale ( $\sim 10^7$  yr). However, the subsequent mass accretion from larger spatial scales may change the global angular momentum in the case of CCA, and thus the jet-launching direction can change from the current direction on longer timescales. This idea is supported by the observed radio morphology: while the radio axis within 1<sup>''</sup> ( $< 1$  kpc) is similar to the current jet axis (Taylor & Vermeulen 1996; Silver et al. 1998; Walker et al. 2000; Asada et al. 2006), the radio lobes/bubbles on kiloparsec scales are misaligned with the inner radio axis (Pedlar et al. 1990). The change in the jet direction, as well as spreading energy over large volumes by buoyant bubbles (Zhang et al. 2018), helps to heat up the galactic halo or cluster atmosphere efficiently and globally (Meece et al. 2017; Cielo et al. 2018), which can mitigate the fact that radio-mode feedback tends to be efficient only in the jet direction.

Even though our observations have not reached the spatial scale of the putative torus for the AGN unification scheme ( $\sim 1$ –10 pc), the observed molecular gas (in particular HCN(3–2) and HCO<sup>+</sup>(3–2)) shows a central concentration. It seems to be reasonable to assume that the molecular gas disk reaches the parsec scale. As we discussed in Section 3.2, we detected the absorption lines of HCN(3–2) and HCO<sup>+</sup>(3–2) only at blueshifted velocities. The absence of a redshifted absorption feature suggests that the molecular gas disk at the parsec scale, where the gas is likely infalling to the AGN, should not intercept our line of sight toward the AGN. In order to realize this, the molecular gas disk must be thin ( $h < r$  where  $h$  is the disk height and  $r$  is the disk radius) since we are viewing the AGN from a relatively large angle ( $65^{\circ} \pm 15^{\circ}$ : Fujita & Nagai 2017). From the viewpoint of AGN unification, NGC 1275 was originally classified as a narrow-line radio galaxy or Seyfert 2, which required obscuration of the central engine by the putative torus. However, the broad H $\alpha$  wing was later identified and NGC 1275 was classified as a Seyfert 1.5/LINER (Sosa-Brito et al. 2001; Véron-Cetty & Véron 2006). Broad H $\beta$  emission with a velocity FWHM of 4150–6000 km s<sup>−1</sup> as well as Pa $\alpha$  and C IV have also recently been detected (Punsly et al. 2018). Those detections of broad emissions lines are consistent with the presence of a thin disk as suggested by our observations. The thin disk was also reported in another low-luminosity AGN, NGC 1097 (Izumi et al. 2017). Izumi et al. (2017) suggested that a thinner disk in NGC 1097 than in NGC 1068 (Imanishi et al. 2018) arose as the result of its low luminosity ( $L_{\text{bol}} = 8.6 \times 10^{41}$  erg s<sup>−1</sup>; Nemmen et al. 2006), which is supported by theoretical predictions (e.g., Elitzur & Shlosman 2006). It is not clear whether the relatively high luminosity of NGC 1275 ( $L_{\text{bol}} = 4 \times 10^{44}$  erg s<sup>−1</sup>; Levinson et al. 1995) can be explained by the same mechanism. We need more samples to improve our understanding of the thickness of the disk/torus.

Hitomi Collaboration et al. (2018) has recently reported the detection of Fe K $\alpha$  line emission associated with the AGN of NGC 1275. The observed velocity width of Fe K $\alpha$  is  $\sim 500$ –1600 km s<sup>−1</sup>. This velocity width suggests that the fluorescing matter is located at a distance of  $\sim 1.4$ –14 pc from the black hole, if we attribute it to the Keplerian rotation velocity of a black hole of mass  $8 \times 10^8 M_{\odot}$ . The absence of variability over 10 years in the emission observed by *Hitomi*, *XMM-Newton*, and *Chandra* also supports the inferred distance of the fluorescing matter. The small equivalent width of the Fe K $\alpha$  line suggests that the fluorescing matter of NGC 1275 is gas with a relatively low column density and/or low covering fraction as compared to other Seyfert galaxies. Hitomi Collaboration et al. concluded that the source of the Fe K $\alpha$

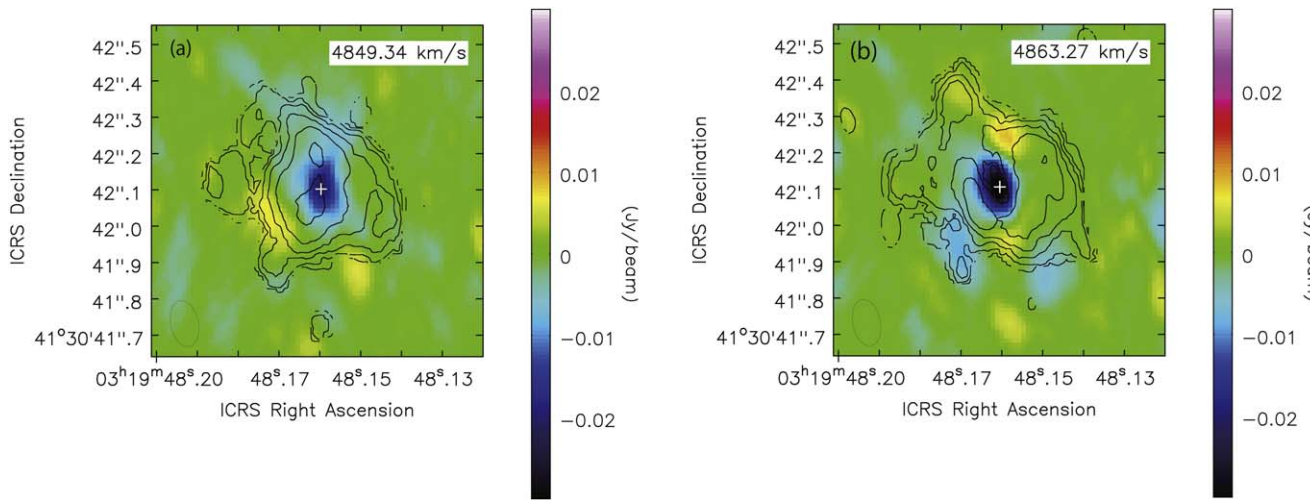


**Figure 8.** (a) Contours of the HCN(3–2) moment 0 map overlaid on the HCN(3–2) intensity map at  $v = 4849 \text{ km s}^{-1}$ . (b) Contours of the HCO<sup>+</sup>(3–2) moment 0 map overlaid on the HCO<sup>+</sup>(3–2) intensity map at  $v = 4863 \text{ km s}^{-1}$ . The plus sign in both figures indicates the location of the AGN.

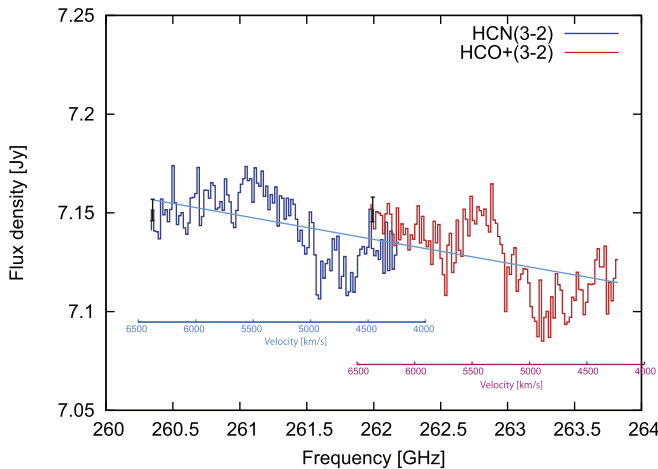


**Figure 9.** (a) The HCN(3–2) (blue) and HCO<sup>+</sup>(3–2) (red) spectra measured on the continuum-unsubtracted images. The scales indicated in cyan and magenta correspond to the velocity for the HCN(3–2) and HCO<sup>+</sup>(3–2) lines, respectively. The flux was calculated within an ellipse ( $0''.15 \times 0''.21$ ) slightly larger than the beam shape to cover all the emissions. Uncertainties are plotted as  $\pm 1\sigma$ . Estimation of uncertainties is explained in the text (see Section 2). To highlight the spectral features, we also show the power-law fit indicated by the cyan line. The fit was done using all spectral channels in both the HCN(3–2) and HCO<sup>+</sup>(3–2) data. The fitted power-law index is  $-0.44$ . Note that there is a slight offset between the HCN(3–2) and HCO<sup>+</sup>(3–2) data on the y-axis at the overlapping frequencies. The difference is  $\sim 0.15\%$  of the averaged flux density. This is probably due to the error in absolute amplitude calibration.

line is a molecular torus or a rotating molecular disk with low covering fraction, which probably extends from a parsec to a scale of hundreds of parsecs. An intriguing comparison is that the velocity width of the HCN(3–2) and HCO<sup>+</sup>(3–2) does not exceed  $\sim 600 \text{ km s}^{-1}$  while the velocity width of Fe K $\alpha$  is  $\sim 500\text{--}1600 \text{ km s}^{-1}$ . Part of the fluorescing matter can be our observed gas disk, but the higher-velocity side of the Fe K $\alpha$  emission can originate in other sources, perhaps the inner part of the disk, e.g., the [F II] emitters (Scharwächter et al. 2013) or a free-free absorber (Walker et al. 2000; Fujita & Nagai 2017).

#### 4.3. Origin of Absorption Feature

The absorption feature is detected at  $v \sim 4600\text{--}4900 \text{ km s}^{-1}$  in both HCN(3–2) and HCO<sup>+</sup>(3–2). The absorbers must be

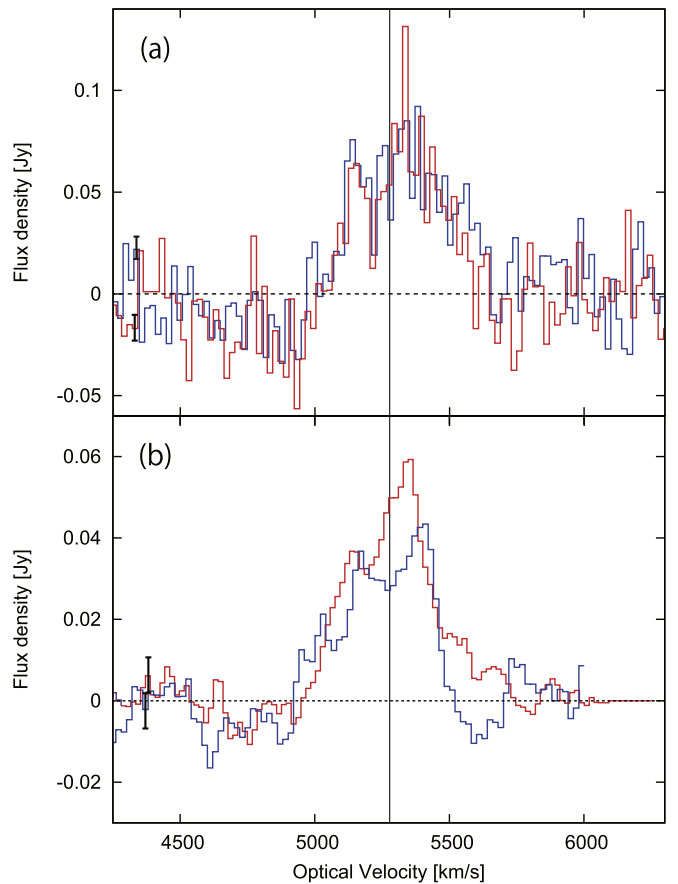


**Figure 10.** Comparison of the HCN(3–2) and HCO<sup>+</sup>(3–2) spectra. (a) The same as Figure 7(a). (b) The HCN(3–2) (red) and HCO<sup>+</sup>(3–2) (blue) spectra of the archival data. The vertical line indicates the systemic optical velocity of  $5624 \text{ km s}^{-1}$ . Uncertainties are plotted as  $\pm 1\sigma$  in the panel. Estimation of uncertainties is explained in the text (see Section 2).

located somewhere between the observer and the AGN of NGC 1275. The absorption against the continuum flux is at most  $\sim 40 \text{ mJy beam}^{-1}$  (or  $\sim 0.6\%$  attenuation), which corresponds to an optical depth of 0.0057. The total H<sub>2</sub> column density of the absorbers is calculated as about  $2.3 \times 10^{22} \text{ cm}^{-2}$  using Equation (2) of Sanhueza et al. (2012). Here we assume

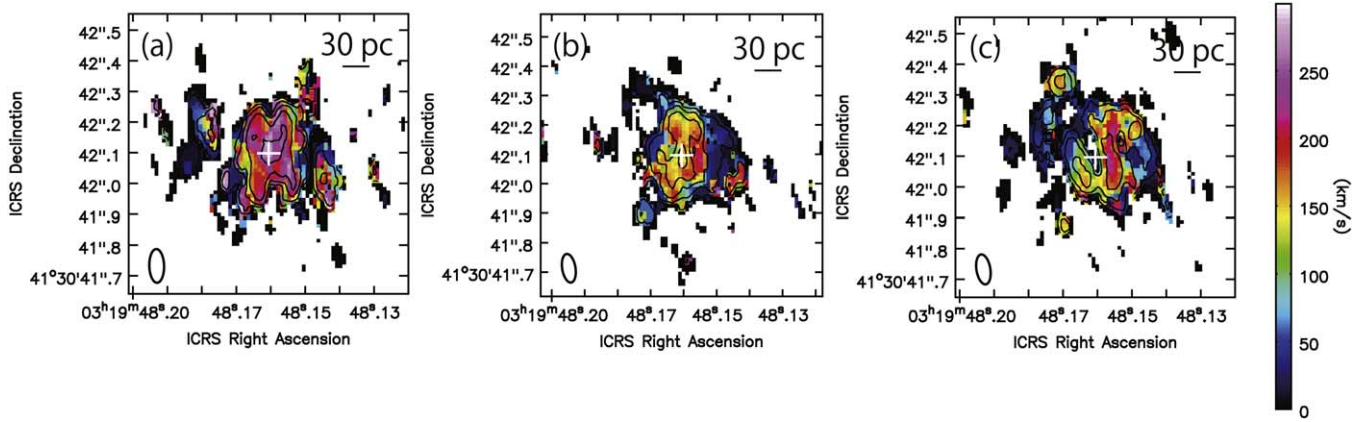


**Figure 11.** Contours of the moment 0 map overlaid on the colored moment 2 map for (a) CO(2–1), (b) HCN(3–2), and (c) HCO<sup>+</sup>(3–2). The maps are made with the Briggs weighting and a robust parameter of 0.5. Contour levels of (a), (b), and (c) are the same as for Figures 1(b), 5(b), and 6(b), respectively.

an excitation temperature of 100 K and an HCN-to-H<sub>2</sub> conversion factor of  $10^{-9}$ . We adopt this conversion factor based on the estimates of abundance ratio in the Galactic circumnuclear disk  $((0.2\text{--}4.1) \times 10^{-9}$ ; Smith & Wardle 2014) and in the dense molecular outflow in Mrk 231  $(0.5 \times 10^{-9}$ ; Aalto et al. 2015).

What is the origin of the absorbers? The background continuum emission comes mostly from the jet of  $\sim 1.2$  pc length (Nagai et al. 2010, 2014), while the extended radio emission in the 10-pc to 10-kpc scale (Romney et al. 1995; Silver et al. 1998; Pedlar et al. 1990; Asada et al. 2006), is negligibly small at this frequency (e.g., Silver et al. 1998). Thus, the absorbers are likely located between the observers and the innermost jet with a projected size of about 1.2 pc. The beam filling factor of the jet is about  $10^{-3}$ . Thus, it is very unlikely that a gas clump at a large distance from the AGN causes the absorptions. It is natural to expect that the absorptions are associated with the clouds close to the nucleus. Since the absorbers are blueshifted from the systemic velocity by  $\sim 300\text{--}600$  km s<sup>-1</sup>, they must be moving toward us.

One promising candidate is outflowing materials associated with the approaching side of the radio jet. The approaching jet is moving toward the south, and its total extent is about 1.2 pc (Nagai et al. 2017). Nagai et al. (2017) and Kino et al. (2018) found an abrupt change in the position of the hotspot of the southern jet in 2015–2016 with an enhancement of polarized emission. This hotspot motion, as well as the enhancement of the polarization, can be caused by interaction between the jet and a dense ambient medium, probably a dense gas clump with a size of  $\sim 0.1$  pc. The dense cloud can be expelled from the AGN by this interaction (e.g., Wagner et al. 2012). We speculate that the outflowing absorbers are candidates for the dense cloud. Such a jet–ISM interaction was also identified in the compact radio jet of 4C 12.50 as HI absorption by VLBI observations (Morganti et al. 2013). Assuming a spherical clump with a radius of 0.1 pc, we obtain the total gas mass of the cloud as  $\sim 3 M_{\odot}$  and the H<sub>2</sub> gas density as  $\sim 7.5 \times 10^4$  cm<sup>-3</sup>. This gas density is in agreement with that estimated from observations of Faraday rotation under the equipartition condition within a factor of 4 (Nagai et al. 2017) and with that estimated from the hotspot dynamics within its uncertainty (Kino et al. 2018). This gas mass can be a lower limit if the clump has been elongated by the jet interaction, as seen in 4C 12.50. Alternatively, the absorber could be a molecular

outflow expelled from the innermost region of the CND by the radiation pressure from the AGN. The observed velocity ( $\sim 300\text{--}600$  km s<sup>-1</sup>) is in fact consistent with that predicted by numerical simulations (Wada 2015). Further observations along other lines may help to better understand the origin of the absorber. In particular, a shock tracer (e.g., SiO) would be detected if the absorber is associated with the jet–ISM interaction.

Previous VLBI observations (Nagai et al. 2017; Kino et al. 2018) suggest that the interaction between the jet and the cloud started in late 2015. The archival data shown in Section 3.2 were taken in 2015 June when the jet interaction had not started or just started. Therefore, it is natural that the absorption lines are less obvious in the archival data.

One may ask why the absorption feature is not detected for the CO(2–1) line. Although the detailed physical mechanism is not clear, several studies have argued that the harsh environment in the close vicinity of the AGN and the influence of the radio jet can increase the HCN or HCO<sup>+</sup> transitions. Meijerink et al. (2011) modeled the intensity ratio of molecular species under the condition of strong cosmic-ray and mechanical heating. For the condition of strong mechanical heating, the HCN/CO intensity ratio increases, and this trend can be boosted, depending on the rate of cosmic-ray heating. Harada et al. (2013) also reported that the intensity ratio of HCN/CO can be larger than unity in the region where the X-ray irradiation is strong. This might explain the absence of CO(2–1) absorption lines since the dense cloud could be mechanically heated by the jet interaction and could also be strongly irradiated by cosmic rays and X-rays from the AGN. The enhancement of HCN and HCO<sup>+</sup> was also reported in the outflow of Mrk 231 (Aalto et al. 2015) and NGC 253 (Walter et al. 2017). One intriguing comparison is that Michiyama et al. (2018) reported the detection of HCN(1–0) and HCO<sup>+</sup>(1–0) emission in the outflow from the southern nucleus of the merging galaxy NGC 3256, where a low-luminosity AGN is located. On the other hand, HCN(1–0) and HCO<sup>+</sup>(1–0) are undetected in the outflow from the northern nucleus, where there is no AGN signature. They claimed that the enhancement of HCN(1–0) and HCO<sup>+</sup>(1–0) emissions is caused by the formation of dense clumps associated with the jet–ISM interaction, possibly via shocks.

The main disk emission shows a double-peak structure in the HCO<sup>+</sup>(3–2) spectrum for both our data and archival data (see

Figures 7 and 10). This spectral shape was not observed in the previous single-dish observations (Bayet et al. 2011). The deficit between the two peaks in the  $\text{HCO}^+$  spectrum is possibly caused by the absorption, which is evident in the spectrum only at the image center, where the AGN is located (see Figure 7(b)). Another absorption-like feature may be seen on the redshifted side at  $v \sim 5750 \text{ km s}^{-1}$ . However, these two features are not seen in the  $\text{HCN}(3-2)$  spectrum. We therefore need confirmation by new observations.

## 5. Black Hole Mass

SMBH mass is a fundamental parameter that determines the AGN physics in connection with the galaxy evolution. It also determines the Schwarzschild radius, which characterizes various physical quantities, such as the Bondi radius and SoI ( $\text{SoI} = GM_{\text{BH}}/\sigma_v^2$  where  $G$  is the gravitational constant,  $M_{\text{BH}}$  is the black hole mass, and  $\sigma_v$  is the central stellar velocity dispersion). Although there is a well-known empirical correlation between the SMBH mass and stellar velocity dispersion ( $M_{\text{BH}}-\sigma$  relation, e.g., Bettoni et al. 2003; Kormendy & Ho 2013; van den Bosch 2016), dynamical measurement of the SMBH mass within the SoI, where the gravitational potential is thought to be dominant, is important in order to derive a robust SMBH mass. Using a stellar velocity dispersion of  $250 \text{ km s}^{-1}$  and  $M_{\text{BH}}$  of  $10^{8.61} M_{\odot}$  (Bettoni et al. 2003), we obtain an SoI of 60 pc. Therefore, molecular gas dynamics revealed by our ALMA observations should help to give a robust constraint on the SMBH mass of NGC 1275. Previously, measurements of the SMBH mass using warm  $\text{H}_2$  gas dynamics were made by Wilman et al. (2005) ( $3 \times 10^8 M_{\odot}$ ) and Scharwächter et al. (2013) ( $8 \times 10^8 M_{\odot}$ ). Although those measurements probed the gas dynamics with a similar spatial resolution to our data, the cold gas ( $\text{CO}(2-1)$ ,  $\text{HCN}(3-2)$ , and  $\text{HCO}^+(3-2)$ ) and warm  $\text{H}_2$  gas can be stratified as we discussed in Section 4.2. Therefore, an independent SMBH mass measurement is still intriguing.

We here model the rotating molecular gas disk traced by the  $\text{CO}(2-1)$  and directly measure the SMBH mass by following a standard procedure as described in Onishi et al. (2017) and Davis et al. (2017, 2018). We use an image cube with natural weighting (see Section 2), which yields a beam size of  $0''.144 \times 0''.077$ . The fitting area is defined here as the central  $1''.55 \times 1''.55$  region and from  $4687$  to  $5580 \text{ km s}^{-1}$ , thus  $129 \times 129 \times 47$  pixels. We model the galaxy mass profile (stars and the SMBH) by using the Multi Gaussian Expansion method (MGE; Emsellem et al. 1994; Cappellari 2002), and include self-gravity of the gas mass by using the publicly available KINEMATIC MOLECULAR SIMULATION (KinMS; Davis et al. 2013) tool.<sup>16</sup>

We use an  $I$ -band archival image from the *Hubble Space Telescope* (*HST*) taken with the F814W filter on the Wide Field Planetary Camera 2 to model the stellar mass component. The *HST* point-spread function (PSF) for this observation was estimated by using TinyTim Version 6.3 (Krist et al. 2011). Before modeling the  $I$ -band luminosity distribution with multiple Gaussians, we mask a region within  $0''.5$  radius from the AGN position, comparable to the size of the PSF (FWHM of  $\sim 0''.8$ ), to avoid any light from the AGN. The dust-attenuated region in the northwest is also masked (see Figure 12). We then take the unmasked region of the image

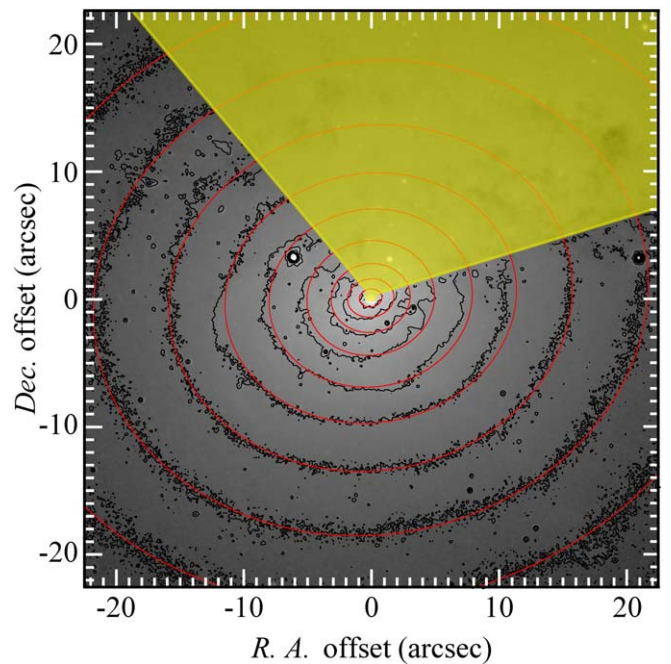


**Figure 12.** A Multi Gaussian Expansion (MGE) model (red contours) overlaid on an *HST*  $I$ -band archival image (F814W filter on Wide Field Planetary Camera 2). We exclude regions highlighted in yellow so to avoid any effect from the AGN (a region within  $0''.5$  radius from the AGN) and from dust attenuation (cone-shaped region in the northwest).

( $100'' \times 100''$ ) and fit the luminosity distribution by using the PSF and the procedure `mge_fit_sectors_regularized`, contained in the `MGE_fit_sectors` IDL package<sup>17</sup> of Cappellari (2002). Figure 12 shows the *HST*  $I$ -band image (grayscale) with the mask (colored in yellow) and the MGE model (red contours) overlaid. A spatially uniform stellar mass-to-light ratio ( $M/L$ ) is then multiplied by the model luminosity profile to create a stellar mass model. The SMBH mass (delta function) is then added at the center. NGC 1275 is known to have a substantial amount of gas at the center, which possibly affects the kinematics (Scharwächter et al. 2013). The molecular gas mass of  $4 \times 10^8 M_{\odot}$ , estimated in Section 4.2, is thus included in the mass model. We also consider a different estimate of the molecular gas mass ( $5 \times 10^7 M_{\odot}$ , also described in Section 4.2) in a different fitting run in order to see the effect.

By using the mass model described above with parameters of  $M/L_I$  and the SMBH mass, a circular velocity curve is calculated from the `MGE_circular_velocity` procedure contained in the `JAM` package of Cappellari (2008), assuming an axisymmetric potential and circular motion. By utilizing KinMS, we take observational effects such as beam smearing and velocity resolution into account, and generate dynamical models of the molecular gas disk. The molecular gas disk is assumed to be in the form of an exponential disk ( $\exp(-r/r_{\text{scale}})$ , where  $r$  corresponds to radius and  $r_{\text{scale}}$  is the scale length). We consider inclination angle, kinematic position angle,  $r_{\text{scale}}$ , gas velocity dispersion (assumed to be uniform over the disk), central position (R.A., decl., and velocity) and the disk luminosity scaling as parameters to describe the disk. For clarification, the gas velocity dispersion given here represents the intrinsic velocity dispersion of gas, such as that

<sup>16</sup> <https://github.com/TimothyADavis/KinMS>

<sup>17</sup> <http://purl.org/cappellari/software>

**Table 4**  
Search Range and Best-fit Values for Model Parameters

Parameter	Search Range	Mol. gas $4 \times 10^8 M_\odot$		Mol. gas $5 \times 10^7 M_\odot$	
		MPFIT Best	Grid Search Error	MPFIT Best	Grid Search Error
SMBH ( $M_\odot$ )	$10^8$ – $10^{10}$	$1.1 \times 10^9$	+0.3, –0.5	$1.2 \times 10^9$	$\pm 3 \times 10^8$
$M/L_I$ ( $M_\odot/L_\odot, I$ )	0.01–1.00	0.050	...	0.050	...
Incl. (deg)	40–65	46	+11, –6	45	+14, –5
PA (deg)	64.0–80.0	74.9	...	75.0	...
$r_{\text{scale}}$ (arcsec)	0.05–0.20	0.12	...	0.12	...
Gas $\sigma$ ( $\text{km s}^{-1}$ )	0–200	22	...	23	...
Central offset: $x$ (arcsec)	–0.2–0.2	0.0	...	0.0	...
$y$ (arcsec)	–0.2–0.2	0.0	...	0.0	...
$v$ ( $\text{km s}^{-1}$ )	–30–30	0	...	0	...
Luminosity scaling	20–50	28.0	...	27.4	...

**Note.** Parameter search region (column 2) and best-fit values (columns 3 and 5) that minimize  $\chi^2$  given by the MPFIT procedure, run for two different molecular gas masses,  $4 \times 10^8 M_\odot$  and  $5 \times 10^7 M_\odot$ . Errors are estimated from a grid search of three parameters (inclination, SMBH mass, and stellar  $M/L_I$ ; see text) and listed in the table (columns 4 and 6). See also Figures 14 and 15 for the residual contours.

due to turbulence. These parameters determine each dynamical model of the molecular gas disk, which is created in the form of a simulated data cube. The simulated cube is then compared to the observed data to evaluate the difference.

We first searched for a set of parameters to minimize the difference between the observed data and the model by using mpfit, which is developed in IDL. The results from two different runs with  $M_{\text{gas}} = 4 \times 10^8 M_\odot$  and  $M_{\text{gas}} = 5 \times 10^7 M_\odot$  are summarized in Table 4.

We then evaluate error budgets for those parameters that have a crucial effect on the SMBH mass. We here select gas disk inclination and the SMBH mass to search the parameters in grids, while other parameters are fixed to the mpfit results.  $M/L_I$  does not affect the SMBH mass for the case of NGC 1275, suggesting that the stellar mass within the fitting area can be ignored (Scharwächter et al. 2013). We confirm this by giving three different  $M/L_I$  values—0.05, 0.50, and 5.00—to see negligible difference (see the lowest panels in Figures 14 and 15). Figure 14 (where  $M_{\text{gas}} = 4 \times 10^8 M_\odot$ ) and Figure 15 ( $M_{\text{gas}} = 5 \times 10^7 M_\odot$ ) show residual contours for the SMBH mass and inclination. The residual is calculated in the same manner as  $\chi^2$ , thus  $(\text{observed} - \text{model})^2 / (\text{rms}_{\text{obs}})^2$ . This residual is useful for judging the fitting results but is not equivalent to  $\chi^2$ , because the neighboring pixels in the observed cube are correlated.

The best-fit values given by mpfit are  $M_{\text{BH}} = 1.1 \times 10^9 M_\odot$ , inclination of  $46^\circ$ ,<sup>18</sup> and  $M/L_I = 0.050 M_\odot/L_\odot, I$  when the molecular gas mass is  $4 \times 10^8 M_\odot$ , and  $M_{\text{BH}} = 1.2 \times 10^9 M_\odot$ , inclination of  $45^\circ$ , and  $M/L_I = 0.050 M_\odot/L_\odot, I$  when it is  $5 \times 10^7 M_\odot$ . Comparisons with what we observed in the form of moment 0, moment 1, and position–velocity diagrams are shown in Figure 13. Our assumption of an exponential disk may not perfectly describe the molecular gas distribution of NGC 1275, but we consider that the model distribution has a negligible effect on the resulting SMBH mass.

The error budget is defined for the SMBH mass and inclination using the residual contours as given in Figures 14 and 15. The large number of pixels ( $129 \times 129 \times 47 \equiv N_{\text{dof}}$ ; number of degrees of freedom excluding the negligible number of free parameters), however, gives a non-negligible standard deviation to  $\chi^2$ , as noted in van den Bosch & van de Ven

(2009) and Mitzkus et al. (2017). In order to avoid unrealistically small errors resulting from this  $\chi^2$ , we follow the approach of van den Bosch & van de Ven (2009) to conservatively increase the  $\Delta\chi^2$  level by multiplying all observed rms noise by  $(2N_{\text{dof}})^{1/4}$ , which is exactly equivalent to decreasing the  $\chi^2$  by  $\sqrt{2N_{\text{dof}}}$ , and thus redefining the confidence level of  $\Delta\chi^2$ . Again, the rescaled residual values are not equivalent to  $\chi^2$ , but we judge the error by allowing all parameters that produce residuals less than  $9 + \chi_{\text{min}}^2$  where  $\chi_{\text{min}}$  is the minimum rescaled residual value during the grid search (940.6 when  $M_{\text{gas}} = 4 \times 10^8 M_\odot$ , 926.6 when  $M_{\text{gas}} = 5 \times 10^7 M_\odot$ ). We obtained the best-fit SMBH mass of  $M_{\text{BH}} = (1.1_{-0.5}^{+0.3}) \times 10^9 M_\odot$  and inclination of  $46_{-11}^{+6}$  deg when the molecular gas mass is  $4 \times 10^8 M_\odot$ , and  $M_{\text{BH}} = (1.2_{-0.6}^{+0.1}) \times 10^9 M_\odot$  and inclination of  $45_{-5}^{+14}$  deg when the molecular gas mass is  $5 \times 10^7 M_\odot$ . We note here that the inclination angle hits the lower limit of the search range, which is given from the stellar mass MGE model. The inclination will at least not reduce the SMBH mass down to zero, simply judging from the residual contours (Figures 14 and 15).

Since the estimated gas mass could be a lower limit because of the lack of short baselines, let us check how the missing mass affects the BH mass estimate. We assume that the whole structure of the disk consists of our detected component with a radius of  $\sim 0''.3$  and a more extended component that is completely filtered out in our observations. We assume that the total gas mass of the inner filament of  $1.8 \times 10^9 M_\odot$  (Lim et al. 2008) is uniformly distributed over the beam area of the observations by Lim et al. ( $3'' \times 2''.7$ ). The missing mass within a radius of  $0''.3$  can be estimated as  $(0''.3 \times 0''.3) \times (1.8 \times 10^9) / (3'' \times 2''.7) = 2 \times 10^7 M_\odot$ . This is well within the SMBH mass error, and thus we conclude the missing mass will not make a big change to our result.

While the derived SMBH mass shows good agreement with that derived from the warm  $\text{H}_2$  gas dynamics (Scharwächter et al. 2013), there is a huge discrepancy with the SMBH mass using the virial estimate from broad emission lines ( $\sim 10^{7.5} M_\odot$ , Koss et al. 2017; Onori et al. 2017). More recently, Punsly et al. (2018) also pointed out that the virial mass estimate can be 10–100 times smaller than the required SMBH mass in order to explain the bolometric luminosity. If we take  $M_{\text{BH}} = 10^{7.5} M_\odot$  and an emission line velocity ( $v_{\text{BLR}}$ ) of  $4500 \text{ km s}^{-1}$ , the radius of the emission region ( $r_{\text{BLR}}$ ) is estimated to be

<sup>18</sup> Inclination angles of  $0^\circ$  and  $90^\circ$  correspond to face-on and edge-on disks, respectively.

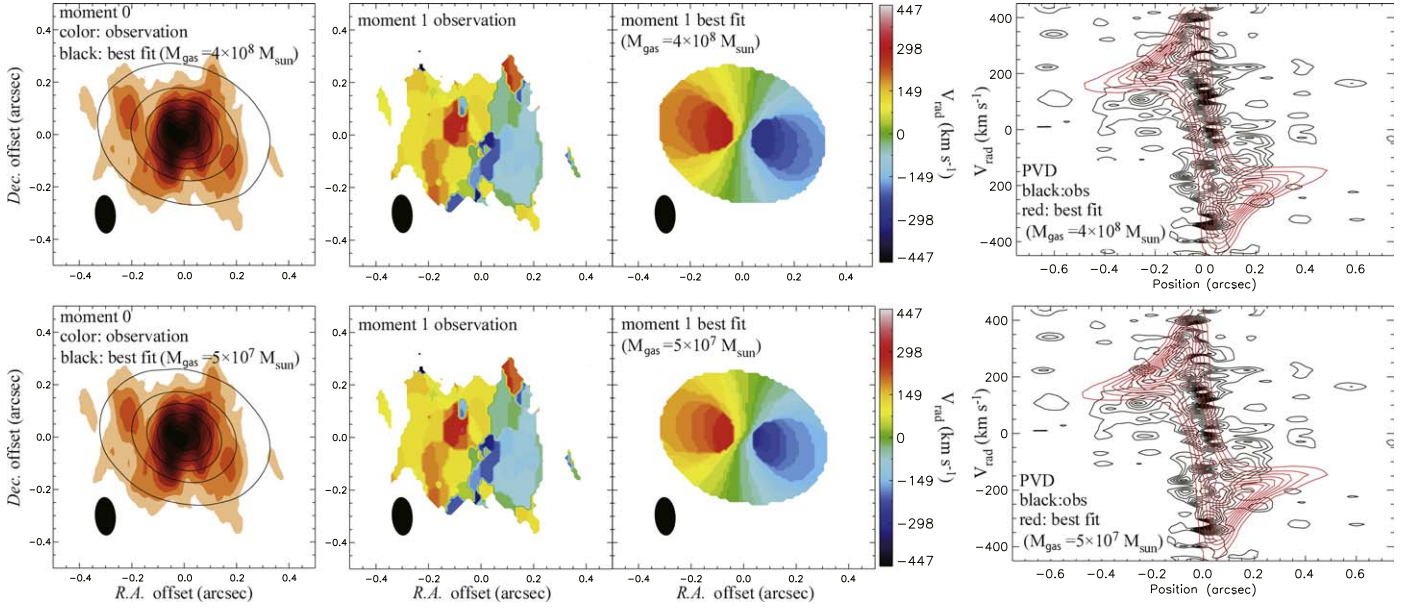


**Figure 13.** Upper panels: comparison between the observation and the best-fit model with a molecular gas mass of  $4 \times 10^8 M_{\odot}$ . Colors are the observed moment 0 map (leftmost), moment 1 map (middle), and position–velocity diagram (rightmost) along the kinematic major axis (position angle of  $75^{\circ}$ ). Red contours in the position–velocity diagram represent the best-fit model. Lower panels: the same as the upper panels but the best-fit model is derived with a molecular gas mass of  $5 \times 10^7 M_{\odot}$ . See Table 4 for the given parameter values.

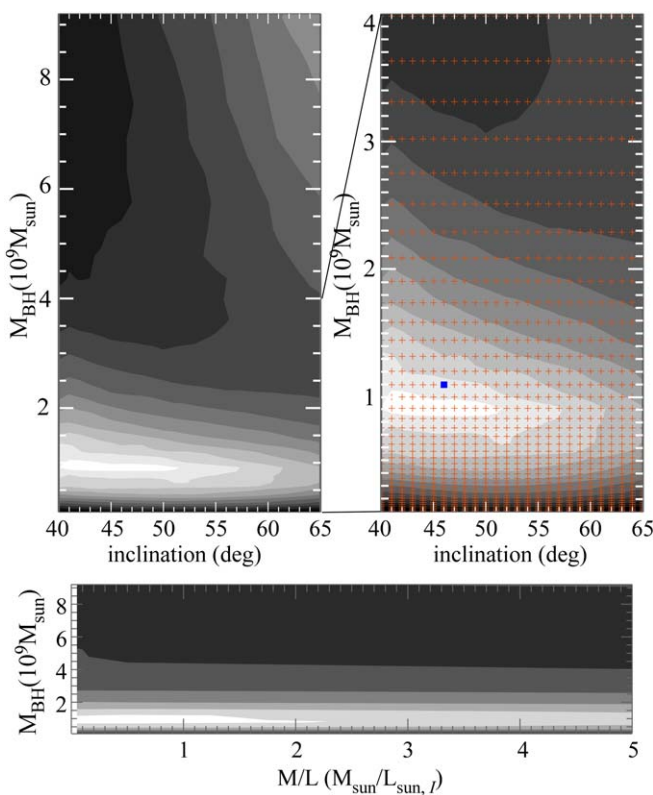


**Figure 14.** Upper panels: residual distribution in a parameter space of inclination ( $40^{\circ}$ – $65^{\circ}$ ) and SMBH mass ( $1 \times 10^8 M_{\odot}$ – $10 \times 10^9 M_{\odot}$ ). Here we assume a molecular gas mass of  $4 \times 10^8 M_{\odot}$  (see Section 4.2). The left panel shows the full parameter space, and the right panel is zoomed into  $M_{\text{BH}} = 1 \times 10^8 M_{\odot}$ – $4 \times 10^9 M_{\odot}$ . The best-fitting parameters obtained by using `mpfit` are highlighted by the blue square. Contours are spaced by 1, 4, 9, 16, 25, 36, 49, 64, 81, 100 plus the minimum residual value reached in this grid search. Lower panel: residual distribution in a parameter space of  $M/L$  ( $0.05$ – $5.00 M_{\odot}/L_{\odot,l}$ ) and SMBH mass ( $1 \times 10^8 M_{\odot}$ – $10 \times 10^9 M_{\odot}$ ). This is to confirm that  $M/L$  does not affect the best-fitting SMBH mass.

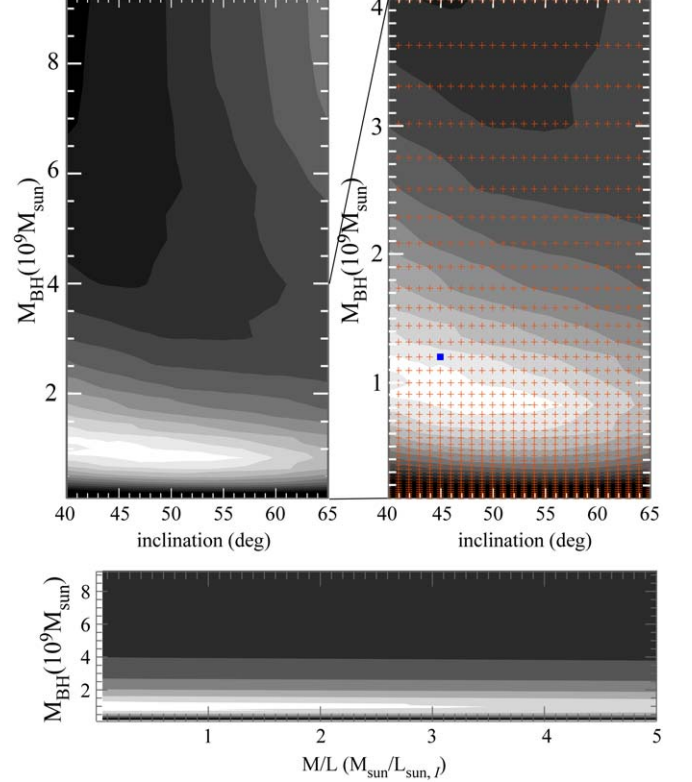


**Figure 15.** Same as Figure 14, but the molecular gas mass is this time assumed to be  $5 \times 10^7 M_{\odot}$  (see Section 4.2).

$\sim 0.007$  pc using the virial relation  $r_{\text{BLR}} = GM_{\text{BH}}/v_{\text{BLR}}^2$ . Netzer & Laor (1993) suggested that the outer edge of the broad-line region (BLR) coincided with the dust sublimation radius of the torus/CND, and reverberation mapping observations also show that the BLR extends out to the dusty torus (Suganuma et al. 2006). Using Equation (1) in Kishimoto et al. (2007) and a UV luminosity

estimated as  $5 \times 10^{42} \text{ erg s}^{-1}$  by Kino et al. (2017), the dust sublimation radius can be estimated as

$$\left[ \frac{r_{\text{sub}}}{\text{pc}} \right] = 0.029 \left[ \frac{L}{5 \times 10^{42} \text{ erg s}^{-1}} \right]^{0.5} \times \left[ \frac{T}{1500 \text{ K}} \right]^{-2.8} \left[ \frac{a}{0.05 \mu\text{m}} \right]^{-0.5}.$$

Here  $L$  is the UV luminosity,  $T$  is the sublimation temperature, and  $a$  is the grain radius. This estimate suggests that there is a discrepancy between  $r_{\text{sub}}$  and  $r_{\text{BLR}}$  by a factor of 4. On the other hand, if we take  $M_{\text{BH}} = 1 \times 10^9 M_{\odot}$ , we then get  $r_{\text{BLR}} = 0.2 \text{ pc}$ , which is more than one order of magnitude larger than  $r_{\text{sub}}$ . Punsly et al. (2018) defined the deprojection factor of the orbital radius of the BLR by taking into account the BL Lac nature of NGC 1275. Assuming a small jet viewing angle, they derived  $M_{\text{BH}} = 1 \times 10^9 M_{\odot}$  from the virial mass estimate using the broad emission lines. However, the assumption of a small viewing angle is not consistent with the estimate of viewing angle using the jet/counter-jet length ratio (Fujita & Nagai 2017) unless the jet angle drastically changes from the jet base to parsec scale. In conclusion, it is difficult to relate the SMBH mass estimate using broad emission lines with the observed nature of NGC 1275. Since NGC 1275 exhibits repeated AGN outbursts, the ionizing photon flux from the accretion disk is probably highly time-variable. This could make the BLR complex, resulting in the discrepancies described above.

We note here that our model still rests on some assumptions that can be explored more carefully. For example, the inclination angle and  $M/L_I$  can have a radial dependence (such as would be the case for a warped disk), and the gas distribution can be better described with multiple Gaussians rather than the exponential disk. Also, additional uncertainties can arise from the imperfectly known distance to the object. We can calculate the proper  $\chi^2$  by comparing the data and the model in the  $(u, v)$  plane. However, we do not probe this in detail and leave these points for our future work.

## 6. Conclusion

We have reported ALMA observations of the CO(2–1), HCN(3–2), and HCO<sup>+</sup>(3–2) lines in NGC 1275. All three lines are detected within the central 100 pc significantly. Only the CO(2–1) emission is also marginally detected on the sub-kiloparsec scale, though it is heavily resolved. The sub-kiloparsec CO(2–1) emission forms filamentary structures, but those cannot be represented by a single infalling stream both morphologically and kinematically. The observed complex behavior of CO(2–1) is consistent with the chaotic cold accretion predicted by recent numerical simulations. The mass accretion rate inferred from the CO gas can be higher than the Bondi accretion rate, which suggests that the cold accretion can be a dominant mechanism in this system.

The main CO(2–1), HCN(3–2), and HCO<sup>+</sup>(3–2) emissions appear to show disk morphology. The velocity distribution shows a gradient at a position angle of  $\sim 70^\circ$ , which can be interpreted as disk rotation. The observed disk morphology and kinematics are similar to those of warm H<sub>2</sub> gas disk found by previous Gemini observations. This suggests that the cold and warm gas phases are distributed at the same radii but are stratified. Intriguingly, the disk rotation axis is approximately the same as the jet axis on the sub-

parsec scale. This may indicate that the cold gas disk is physically connected to the further inner accretion disk, which is responsible for jet launching, and thus the cold accretion may play an important role in characterizing the AGN activity. Higher spatial resolution would be crucial to study the nature of cold accretion in the further inner region, as well as the connection with the FFA disk identified by VLBI observations.


Overall, our observations suggest that cold accretion can play an important role in AGN feeding in representative nearby BCGs, which are thought to be the most massive galaxies and hosts of the most massive SMBHs in the local universe. A better angular resolution with more extended ALMA configurations will allow us to resolve the Bondi radius ( $\sim 10 \text{ pc}$ ) of NGC 1275 in future cycles, which is crucial to better understand the physics of black hole accretion.

We detected the blueshifted absorption lines in the HCN(3–2) and HCO<sup>+</sup> spectra and confirmed them with the archival HCO<sup>+</sup>(3–2) spectrum. The most probable candidate for the absorber is a dense gas clump interacting with the radio jet, which was recently identified as the abrupt change in the hotspot motion by VLBI observations. Alternatively, the absorber could be outflowing gas expelled from the innermost CNB by radiation pressure. Time variability of the absorption feature would be detected if such an interaction is underway. This will be verified with future monitoring observations.

Using the observed velocity structure and archival *HST* data, we measured the dynamical mass of the SMBH. The measured value is  $1 \times 10^9 M_{\odot}$ , which agrees with the dynamical measurement using the warm H<sub>2</sub> gas but disagrees with the virial mass estimate using broad emission lines. The discrepancies can arise from the complexity of the BLR structure, which is possibly related to the violent time variation of AGN activity in NGC 1275. Similar comparisons with other AGNs would help us to figure out the cause. Increasing the sample of SMBH mass estimates by molecular gas dynamics with ALMA (e.g., Barth et al. 2016; Boizelle et al. 2019; Smith et al. 2019) is one of key approaches to shed light on this problem.

We thank the referee for constructive comments. This paper makes use of the following ALMA data: ADS/JAO.ALMA#2017.0.01257.S and ADS/JAO.ALMA#2013.1.01102.S. ALMA is a partnership of ESO (representing its member states), NSF (USA) and NINS (Japan), together with NRC (Canada), MOST and ASIAA (Taiwan), and KASI (Republic of Korea), in cooperation with the Republic of Chile. The Joint ALMA Observatory is operated by ESO, AUI/NRAO and NAOJ. H.N. is supported by JSPS KAKENHI grant No. JP18K03709. N.K. is supported by JSPS KAKENHI grant No. JP16K17670. Y.F. is supported by JSPS KAKENHI grant No. JP18K03647. M.K. is supported by JSPS KAKENHI grant Nos. JP18K03656 and JP18H03721. K.O. acknowledges support from Shimadzu Science Foundation and is supported by JSPS KAKENHI grant No. JP19K14763. J.L. acknowledges support from the Research Grants Council of Hong Kong through grant 17304817 for the conduct of this work. W.F. acknowledges support from the Smithsonian Institution and the Chandra HRC program through NASA contract NAS8-03060. This work is supported by grant MOST 107-2119-M-001-026- (Y.O.).

## ORCID iDs

H. Nagai  <https://orcid.org/0000-0003-0292-3645>  
K. Onishi  <https://orcid.org/0000-0002-0997-1060>

N. Kawakatu <https://orcid.org/0000-0003-2535-5513>  
 Y. Fujita <https://orcid.org/0000-0003-0058-9719>  
 M. Kino <https://orcid.org/0000-0002-2709-7338>  
 Y. Fukazawa <https://orcid.org/0000-0002-0921-8837>  
 J. Lim <https://orcid.org/0000-0003-4220-2404>  
 W. Forman <https://orcid.org/0000-0002-9478-1682>  
 K. Nakanishi <https://orcid.org/0000-0002-6939-0372>  
 K. Wajima <https://orcid.org/0000-0003-3823-7954>  
 Y. Ohyama <https://orcid.org/0000-0001-9490-3582>

## References

- Aalto, S., Garcia-Burillo, S., Muller, S., et al. 2015, *A&A*, 574, A85  
 Abdo, A. A., Ackermann, M., Ajello, M., et al. 2009, *ApJ*, 699, 31  
 Alatalo, K., Davis, T. A., Bureau, M., et al. 2013, *MNRAS*, 432, 1796  
 Andreani, P., Carpenter, J., Diaz Trigo, M., et al. 2018, ALMA Cycle 6 Proposer's Guide (San Pedro de Atacama: ALMA)  
 Antonucci, R. 1993, *ARA&A*, 31, 473  
 Asada, K., Kamenno, S., Shen, Z.-Q., et al. 2006, *PASJ*, 58, 261  
 Barai, P., Proga, D., & Nagamine, K. 2012, *MNRAS*, 424, 728  
 Barth, A. J., Boizelle, B. D., Darling, J., et al. 2016, *ApJL*, 822, L28  
 Bayet, E., Viti, S., Hartquist, T. W., & Williams, D. A. 2011, *MNRAS*, 417, 627  
 Bettoni, D., Falomo, R., Fasano, G., & Govoni, F. 2003, *A&A*, 399, 869  
 Blandford, R. D., & Znajek, R. L. 1977, *MNRAS*, 179, 433  
 Boizelle, B. D., Barth, A. J., Walsh, J. L., et al. 2019, *ApJ*, 881, 10  
 Briggs, D. 1995, PhD thesis, New Mexico Institute of Mining and Technology  
 Cappellari, M. 2002, *MNRAS*, 333, 400  
 Cappellari, M. 2008, *MNRAS*, 390, 71  
 Carilli, C. L., Perley, R. A., Dhawan, V., et al. 2019, *ApJL*, 874, L32  
 Churazov, E., Brüggen, M., Kaiser, C. R., Böhringer, H., & Forman, W. 2001, *ApJ*, 554, 261  
 Cielo, S., Babul, A., Antonuccio-Delogu, V., Silk, J., & Volonteri, M. 2018, *A&A*, 617, A58  
 Davis, T. A., Bureau, M., Cappellari, M., Sarzi, M., & Blitz, L. 2013, *Natur*, 494, 328  
 Davis, T. A., Bureau, M., Onishi, K., et al. 2017, *MNRAS*, 468, 4675  
 Davis, T. A., Bureau, M., Onishi, K., et al. 2018, *MNRAS*, 473, 3818  
 De Lucia, G., Springel, V., White, S. D. M., Croton, D., & Kauffmann, G. 2006, *MNRAS*, 366, 499  
 Downes, D., & Solomon, P. M. 1998, *ApJ*, 507, 615  
 Dubinski, J. 1998, *ApJ*, 502, 141  
 Dutson, K. L., Edge, A. C., Hinton, J. A., et al. 2014, *MNRAS*, 442, 2048  
 Eitzur, M., & Shlosman, I. 2006, *ApJL*, 648, L101  
 Emsellem, E., Monnet, G., & Bacon, R. 1994, *A&A*, 285, 723  
 EnBlin, T. A., & Vogt, C. 2006, *A&A*, 453, 447  
 Fabian, A. C., Johnstone, R. M., Sanders, J. S., et al. 2008, *Natur*, 454, 968  
 Fabian, A. C., Sanders, J. S., Allen, S. W., et al. 2003, *MNRAS*, 344, L43  
 Fabian, A. C., Walker, S. A., Pinto, C., Russell, H. R., & Edge, A. C. 2015, *MNRAS*, 451, 3061  
 Fanaroff, B. L., & Riley, J. M. 1974, *MNRAS*, 167, 31P  
 Forman, W., Jones, C., Churazov, E., et al. 2007, *ApJ*, 665, 1057  
 Fujita, Y., Kawakatu, N., Shlosman, I., & Ito, H. 2016, *MNRAS*, 455, 2289  
 Fujita, Y., & Nagai, H. 2017, *MNRAS*, 465, L94  
 Fujita, Y., Okabe, N., Sato, K., et al. 2013, *PASJ*, 65, L15  
 Gaspari, M., Ruszkowski, M., & Oh, S. P. 2013, *MNRAS*, 432, 3401  
 Gaspari, M., Temi, P., & Brighenti, F. 2017, *MNRAS*, 466, 677  
 Gendron-Marsolais, M., Hlavacek-Larrondo, J., Martin, T. B., et al. 2018, *MNRAS*, 479, L28  
 Giovannini, G., Savolainen, T., Orienti, M., et al. 2018, *NatAs*, 2, 472  
 Hamer, S. L., Edge, A. C., Swinbank, A. M., et al. 2014, *MNRAS*, 437, 862  
 Harada, N., Thompson, T. A., & Herbst, E. 2013, *ApJ*, 765, 108  
 Hatch, N. A., Crawford, C. S., Johnstone, R. M., & Fabian, A. C. 2006, *MNRAS*, 367, 433  
 Hitomi Collaboration, Aharonian, F., Akamatsu, H., et al. 2018, *PASJ*, 70, 13  
 Hiura, K., Nagai, H., Kino, M., et al. 2018, *PASJ*, 70, 83  
 Hodgson, J. A., Rani, B., Lee, S.-S., et al. 2018, *MNRAS*, 475, 368  
 Imanishi, M., Nakanishi, K., Izumi, T., & Wada, K. 2018, *ApJL*, 853, L25  
 Izumi, T., Kawakatu, N., & Kohno, K. 2016, *ApJ*, 827, 81  
 Izumi, T., Kohno, K., Fathi, K., et al. 2017, *ApJL*, 845, L5  
 Kawakatu, N., & Wada, K. 2008, *ApJ*, 681, 73  
 Kino, M., Ito, H., Wajima, K., et al. 2017, *ApJ*, 843, 82  
 Kino, M., Wajima, K., Kawakatu, N., et al. 2018, *ApJ*, 864, 118  
 Kishimoto, M., Hönig, S. F., Beckert, T., & Weigelt, G. 2007, *A&A*, 476, 713  
 Kormendy, J., & Ho, L. C. 2013, *ARA&A*, 51, 511  
 Koss, M., Trakhtenbrot, B., Ricci, C., et al. 2017, *ApJ*, 850, 74  
 Krist, J. E., Hook, R. N., & Stoehr, F. 2011, *Proc. SPIE*, 8127, 81270J  
 Lazareff, B., Castets, A., Kim, D.-W., et al. 1989, *ApJL*, 336, L13  
 Levinson, A., Laor, A., & Vermeulen, R. C. 1995, *ApJ*, 448, 589  
 Lim, J., Ao, Y., & Dinh-V-Trung 2008, *ApJ*, 672, 252  
 McConnell, N. J., & Ma, C.-P. 2013, *ApJ*, 764, 184  
 Meece, G. R., Voit, G. M., & O'Shea, B. W. 2017, *ApJ*, 841, 133  
 Meijerink, R., Spaans, M., Loenen, A. F., & van der Werf, P. P. 2011, *A&A*, 525, A119  
 Michiyama, T., Iono, D., Sliwa, K., et al. 2018, *ApJ*, 868, 95  
 Mirabel, I. F., Sanders, D. B., & Kazes, I. 1989, *ApJL*, 340, L9  
 Mitzkus, M., Cappellari, M., & Walcher, C. J. 2017, *MNRAS*, 464, 4789  
 Morganti, R., Fogasy, J., Paragi, Z., Oosterloo, T., & Orienti, M. 2013, *Sci*, 341, 1082  
 Myers, P. C. 1978, *ApJ*, 225, 380  
 Nagai, H., Chida, H., Kino, M., et al. 2016, *AN*, 337, 69  
 Nagai, H., Fujita, Y., Nakamura, M., et al. 2017, *ApJ*, 849, 52  
 Nagai, H., Haga, T., Giovannini, G., et al. 2014, *ApJ*, 785, 53  
 Nagai, H., Orienti, M., Kino, M., et al. 2012, *MNRAS*, 423, L122  
 Nagai, H., Suzuki, K., Asada, K., et al. 2010, *PASJ*, 62, L11  
 Narayan, R., & Yi, I. 1994, *ApJL*, 428, L13  
 Nemmen, R. S., Storchi-Bergmann, T., Yuan, F., et al. 2006, *ApJ*, 643, 652  
 Netzer, H., & Laor, A. 1993, *ApJL*, 404, L51  
 Okuda, T., Kohno, K., Iguchi, S., & Nakanishi, K. 2005, *ApJ*, 620, 673  
 Onishi, K., Iguchi, S., Davis, T. A., et al. 2017, *MNRAS*, 468, 4663  
 Onori, F., Ricci, F., La Franca, F., et al. 2017, *MNRAS*, 468, L97  
 Papadopoulos, P. P., van der Werf, P., Xilouris, E., Isaak, K. G., & Gao, Y. 2012, *ApJ*, 751, 10  
 Pedlar, A., Ghataure, H. S., Davies, R. D., et al. 1990, *MNRAS*, 246, 477  
 Perlman, E. S., Mason, R. E., Packham, C., et al. 2007, *ApJ*, 663, 808  
 Pizzolato, F., & Soker, N. 2010, *MNRAS*, 408, 961  
 Pringle, J. E. 1981, *ARA&A*, 19, 137  
 Punsly, B., Marziani, P., Bennert, V. N., Nagai, H., & Gurwell, M. A. 2018, *ApJ*, 869, 143  
 Romney, J. D., Benson, J. M., Dhawan, V., et al. 1995, *PNAS*, 92, 11360  
 Rose, T., Edge, A. C., Combes, F., et al. 2019, *MNRAS*, 485, 229  
 Ruffa, I., Prandoni, I., Laing, R. A., et al. 2019, *MNRAS*, 484, 4239  
 Russell, H. R., McDonald, M., McNamara, B. R., et al. 2017, *ApJ*, 836, 130  
 Russell, H. R., McNamara, B. R., Fabian, A. C., et al. 2016, *MNRAS*, 458, 3134  
 Salomé, P., Combes, F., Edge, A. C., et al. 2006, *A&A*, 454, 437  
 Salomé, P., Combes, F., Revaz, Y., et al. 2008, *A&A*, 484, 317  
 Salomé, P., Combes, F., Revaz, Y., et al. 2011, *A&A*, 531, A85  
 Sanders, J. S., Fabian, A. C., Allen, S. W., et al. 2004, *MNRAS*, 349, 952  
 Sanhueza, P., Jackson, J. M., Foster, J. B., et al. 2012, *ApJ*, 756, 60  
 Scharwächter, J., McGregor, P. J., Dopita, M. A., & Beck, T. L. 2013, *MNRAS*, 429, 2315  
 Seyfert, C. K. 1943, *ApJ*, 97, 28  
 Shakura, N. I., & Sunyaev, R. A. 1973, *A&A*, 24, 337  
 Silver, C. S., Taylor, G. B., & Vermeulen, R. C. 1998, *ApJ*, 502, 229  
 Smith, I. L., & Wardle, M. 2014, *MNRAS*, 437, 3159  
 Smith, M. D., Bureau, M., Davis, T. A., et al. 2019, *MNRAS*, 485, 4359  
 Solomon, P. M., & Vanden Bout, P. A. 2005, *ARA&A*, 43, 677  
 Sosa-Brito, R. M., Tacconi-Garman, L. E., Lehnert, M. D., & Gallimore, J. F. 2001, *ApJS*, 136, 61  
 Suganuma, M., Yoshii, Y., Kobayashi, Y., et al. 2006, *ApJ*, 639, 46  
 Suzuki, K., Nagai, H., Kino, M., et al. 2012, *ApJ*, 746, 140  
 Tan, J. C., Beuther, H., Walter, F., & Blackman, E. G. 2008, *ApJ*, 689, 775  
 Taylor, G. B., & Vermeulen, R. C. 1996, *ApJL*, 457, L69  
 Tonini, C., Beryk, M., Croton, D., Maraston, C., & Thomas, D. 2012, *ApJ*, 759, 43  
 Tremblay, G. R., Onk, J. B. R., Combes, F., et al. 2016, *Natur*, 534, 218  
 van den Bosch, R. C. E. 2016, *ApJ*, 831, 134  
 van den Bosch, R. C. E., & van de Ven, G. 2009, *MNRAS*, 398, 1117  
 Véron-Cetty, M.-P., & Véron, P. 2006, *A&A*, 455, 773  
 Wada, K. 2015, *ApJ*, 812, 82  
 Wagner, A. Y., Bicknell, G. V., & Umemura, M. 2012, *ApJ*, 757, 136  
 Walker, R. C., Dhawan, V., Romney, J. D., Kellermann, K. I., & Vermeulen, R. C. 2000, *ApJ*, 530, 233  
 Walter, F., Bolatto, A. D., Leroy, A. K., et al. 2017, *ApJ*, 835, 265  
 Warmels, R., Biggs, A., Cortes, P., et al. 2018, ALMA Technical Handbook, ALMA Doc. 6.3, ver. 1.0 (San Pedro de Atacama: ALMA) 978-3-923524-66-2  
 Wilman, R. J., Edge, A. C., & Johnstone, R. M. 2005, *MNRAS*, 359, 755  
 Yuan, F., & Narayan, R. 2014, *ARA&A*, 52, 529  
 Zhang, C., Churazov, E., & Schekochihin, A. A. 2018, *MNRAS*, 478, 4785